Pseudo-2D RANS: A LiDAR-driven mid-fidelity model for simulations of wind farm flows

Cite as: J. Renewable Sustainable Energy 14, 023301 (2022); https://doi.org/10.1063/5.0076739
Submitted: 27 October 2021 • Accepted: 26 February 2022 • Accepted Manuscript Online: 01 March 2022
• Published Online: 17 March 2022

📵 S. Letizia and 📵 G. V. lungo







ARTICLES YOU MAY BE INTERESTED IN

Research on methods for extracting aging characteristics and health status of lithium-ion batteries based on small samples

Journal of Renewable and Sustainable Energy **14**, 024101 (2022); https://doi.org/10.1063/5.0071686

Adaptive fractional order control of doubly fed induction generator based wind energy conversion system under uncertainty

Journal of Renewable and Sustainable Energy **13**, 033311 (2021); https://doi.org/10.1063/5.0041047

Phase-averaged dynamics of a periodically surging wind turbine Journal of Renewable and Sustainable Energy 14, 013305 (2022); https://doi.org/10.1063/5.0076029





Pseudo-2D RANS: A LiDAR-driven mid-fidelity model for simulations of wind farm flows

Cite as: J. Renewable Sustainable Energy 14, 023301 (2022); doi: 10.1063/5.0076739 Submitted: 27 October 2021 · Accepted: 26 February 2022 · Published Online: 17 March 2022







S. Letizia 🕞 and G. V. lungo^{a)} 🕞



AFFILIATIONS

Wind Fluids and Experiments (WindFluX) Laboratory, Mechanical Engineering Department, The University of Texas at Dallas, 800 W Campbell Rd., Richardson, Texas 75080, USA

a) Author to whom correspondence should be addressed: valerio.iungo@utdallas.edu.

ABSTRACT

Next-generation models of wind farm flows are increasingly needed to assist the design, operation, and performance diagnostic of modern wind power plants. Accuracy in the descriptions of the wind farm aerodynamics, including the effects of atmospheric stability, coalescing wakes, and the pressure field induced by the turbine rotors are necessary attributes for such tools as well as low computational costs. The Pseudo-2D RANS model is formulated to provide an efficient solution of the Navier-Stokes equations governing wind-farm flows installed in flat terrain and offshore. The turbulence closure and actuator disk model are calibrated based on wind light detection and ranging measurements of wind turbine wakes collected under different operative and atmospheric conditions. A shallow-water formulation is implemented to achieve a converged solution for the velocity and pressure fields across a farm with computational costs comparable to those of mid-fidelity engineering wake models. The theoretical foundations and numerical scheme of the Pseudo-2D RANS model are provided, together with a detailed description of the verification and validation processes. The model is assessed against a large dataset of power production for an onshore wind farm located in North Texas showing a normalized mean absolute error of 5.6% on the 10-min-averaged active power and 3% on the clustered wind farm efficiency, which represent 8% and 24%, respectively, improvements with respect to the best-performing engineering wake model tested in this work.

Published under an exclusive license by AIP Publishing. https://doi.org/10.1063/5.0076739

I. INTRODUCTION

A deeper understanding of the physical processes governing the operation of modern wind farms is instrumental to enable reduction of the levelized cost of energy (LCOE) and increase in wind energy penetration in the global power system. 1,2 Specifically, many mechanisms governing the aerodynamics of wind turbines immersed in the atmospheric turbulent boundary layer remain still elusive nowadays.³ By extracting kinetic energy from the incoming flow, wind turbines generate wakes, which can persist for several kilometers downstream⁴⁻⁶ and cause power losses and enhanced fatigue loads for downstream wind turbines.^{7,8} Wind industry stakeholders identify turbine wakes as one of the major causes for energy losses for onshore power plants in North America.9 Quantitative studies of wake effects based on the analysis of supervisory control and data acquisition (SCADA) data showed energy losses between 2% and 4% for onshore sites⁷ and 10% to 20% of the annual energy production (AEP) for offshore wind farms. 10 Nonetheless, a recent analysis of data covering ten years of operations for the Lillgrund offshore wind farm (a power plant designed

for power maximization) revealed a reduction in power capture as high as 28% of the nominal capacity.¹

The prediction of wake impact on wind farm performance is complicated by the influence of the atmospheric stability on wake recovery, 12-15 which results in significantly reduced power losses for high turbulence intensity and convective atmospheric conditions compared to low turbulence intensity, stable atmospheric conditions.^{7,16,17} An additional hurdle for predicting wake-induced power losses is represented by the coalescence of multiple wakes, which creates a spatially heterogeneous and highly turbulent flow within the wind farm boundary layer. Furthermore, the pressure field created by the thrust of the rotors induces blockage 18-23 and speedups, 18,24,25 which can significantly impact wind turbine performance, yet generally not modeled in engineering approaches due to the excessive computational burden that a coupled solution of the continuity and momentum equation entails when including the pressure field.

During the past four decades, several wake and wind farm models have been proposed, spanning a breadth of approaches and levels of sophistication. Wake models can be broadly classified into two categories: analytical models and computational fluid mechanics (CFD) methods.² The simplest analytical models assume a top-hat velocity profile and calculate the wake width and velocity deficit based on mass²⁶ or momentum²⁷ conservation. Other analytical wake models assume self-similarity of the wake velocity profiles, in analogy to the shear-flow theory,^{28,29} to predict maximum velocity deficit and wake width as a function of the downstream distance from the turbine rotor.^{30–32} The self-similarity assumption is also at the basis of the Gaussian wake model,³³ and the subsequent evolutions, such as the Ishihara model,³⁴ the elliptic-Gaussian model,³⁵ the Gaussian plume dispersion model,³⁶ the double-Gaussian model,³⁷ and the super-Gaussian models.^{38,39} It is noteworthy that the self-similarity hypothesis is strictly valid only if the wake velocity deficit is significantly smaller than the freestream velocity, which is typically true only in the very far-wake.⁴⁰

The extremely low computational cost and the simple implementation contributed to the popularity of engineering wake models, which are still included in several state-of-the-art tools for wind farm design and modeling. He main drawbacks of most analytical wake models are the need for tuning parameters regulating the wake recovery and the shape of the velocity profiles. He Furthermore, engineering wake models typically require the use of superposition principles in the case of multiple wakes, which introduce a further inaccuracy. Nevertheless, if properly calibrated, these models exhibit a mean absolute error in the prediction of wake power losses smaller than 15% and, unexpectedly, comparable to that of more complex CFD models. 14,47–50

CFD models, especially Reynolds-Averaged Navier–Stokes (RANS) and Large Eddy Simulations (LES), have been increasingly employed to simulate wind farm flows by solving the governing equations for turbulent flows. 51,52 Specifically, LES have provided insightful information into the turbine wake flow physics (see reviews by 53,54) however, their high computational cost ($\sim\!10^3\!-\!10^4$ CPU hours, 2 depending on the Reynolds number 55) represents a serious hindrance for their utilization in computationally intensive tasks, such as online control, real-time diagnostic applications, and layout optimization. Furthermore, the sub-grid model needs to be carefully selected to avoid inconsistent results near the ground, 56 for stratified flows, 57 and in the proximity of the turbines. 2

Although very sensitive to the type of turbulent closure adopted, RANS models have computational costs generally three orders of magnitude smaller than LES.⁵⁸ The time required for a RANS simulation is intrinsically dependent on the simplifying assumption applied to the Navier-Stokes equations and the solver implemented. Linearization of the advection term is a commonly adopted approximation for early RANS models^{59–61} and received renewed interest more recently thanks to the achieved low computational costs. Modern linearized models include FUGA, 62 ORFEUS, 20 the curled wake model. 63 Another popular class of models is the parabolic RANS, where, by leveraging the boundary-layer approximation, computational costs are reduced by solving the RANS equations from the inlet moving in the downstream direction by neglecting the elliptic nature of subsonic flows. The classic models of Liu,⁶⁴ Ainslie,⁶⁵ and UPMWAKE⁶¹ belong to this category. More recently, a parabolic axisymmetric solver for turbine arrays was optimally calibrated based on high-fidelity simulations. 66-68 The commercial tool WakeBlaster⁶⁹ is also a parabolic 3D wind farm model that can solve the flow of a medium-size wind farm in a few seconds.

Furthermore, the curled wake model in his fully linearized version ⁶³ and the newest release ⁷⁰ use a parabolic solution to reduce the computational time. The main drawback of parabolic models is the breakdown of the boundary layer approximation in the near wake ⁴⁰ and the inability to simulate the effects of pressure (namely, blockage and speedups) on the wind field. ²¹

A more detailed flow characterization can be achieved through elliptic RANS models, which solve the full set of RANS equations at the cost of a significantly higher computational requirement. Crespo and Hendández⁷¹ formulated an elliptic implementation of UPMWAKE, whose results showed only slight differences with respect to the original parabolic version. Masson *et al.*⁷² formulated a steady laminar axisymmetric RANS solver based on the actuator disk theory, subsequently enhanced through the inclusion of a turbulence model⁷³ and a 3D formulation.⁷⁴ In an attempt to reduce the dimensionality and, thus, computational burden, several authors resolved the wind farm flow at hub height in a purely 2D fashion, ^{75–78} which however can result in an excessive curvature of the streamlines due to the unphysical vertical confinement.⁷⁹

A crucial aspect of a RANS model is the modeling of the turbulent Reynolds stresses, aimed at capturing the complex role of atmospheric turbulence, blade- and wake-generated turbulence, and wake dynamics, such as wake meandering. The vast majority of the RANS models adopt the linear turbulent eddy viscosity hypothesis, with just a few examples of Reynolds Stress transport and nonlinear eddy viscosity closures. It is worth mentioning that the eddy viscosity approach has been disproved based on theoretical arguments and experimental evidence for flows undergoing rapid distortion, and particularly for the flow near wind turbines. Nevertheless, the eddy viscosity can provide a useful characterization of mean quantities for simple shear flows.

Algebraic closures for turbine wakes specify the value of the turbulent eddy viscosity or mixing length *a priori*, ⁷⁹ based on the Monin–Obukhov similarity theory, ^{20,62–64,74} wake characteristics ⁶⁰ or both. ^{65,69,87} A fairly complex algebraic closure is implemented in the dynamic wake meandering model and includes effects of atmospheric stability, ⁸⁸ shear, and wake-added turbulence. ⁸⁹ Some authors pursued a more data-driven approach by calibrating the turbulence model against LES ⁶⁷ or experimental data collected with light detection and ranging (LiDAR) systems. ^{78,90} The standard two-equation models (namely, $\kappa - \varepsilon$ and $\kappa - \omega$), despite their well-documented accuracy in the solution of other classic fluid mechanics problems, are known to be over-diffusive in the near wake, ^{84,91} where the rapid flow changes, high velocity, and pressure gradients undermine the fundamental assumptions of the eddy viscosity model. ⁸⁶ This has spurred significant research work in the development of advanced turbulence closure for turbine wake flow. ^{58,92–94}

The foregoing appraisal of the capabilities and limitations of the state-of-the-art turbine wake models inspired the formulation of a novel mid-fidelity model for wind farm flows: the Pseudo-2D RANS (P2D-RANS hereinafter). This tool is conceived to provide a comprehensive description of the time-averaged wind farm aerodynamics, including multiple wake interactions and the effects of atmospheric stability and pressure field while keeping the computational costs low enough to simulate a medium-size farm in a few CPU seconds. With these aims, three main novelties are introduced: (i) the 3D flow equations are reduced to a 2D mathematical problem by adopting the

shallow-water model with tailor-made corrections for near-wake vertical fluxes and dispersive terms; (ii) the partially parabolized Navier-Stokes (PPNS) equations are solved by retaining the full elliptic pressure field yet ensuring numerical efficiency of the iterative marching scheme of the numerical solver; and (iii) the turbulence closure and actuator disk model are optimally calibrated based on LiDAR data clustered based on incoming wind speed and turbulence intensity. 15,44 We will show in the following that the P2D-RANS is also capable of accurately simulating highly challenging wind conditions where the pressure field induced by the turbine rotors can modify the incoming wind leading to local speedups, and, in turn, increased power capture, which has been confirmed experimentally. Accuracy of the P2D-RANS is assessed for the case study of an onshore wind farm located in North Texas including 25 2.3 MW turbines. The current implementation of the code can simulate the steady-state operation of the investigated wind farm for a single inflow case in around 80 s on an i5 single-core laptop computer.

The remainder of this manuscript is organized as follows: the first two sections describe the conceptual (Sec. II) and numerical (Sec. III) modeling of the depth-averaged, partially parabolized Navier-Stokes equations. Section IV provides a description of the experimental site and the dataset used for the tuning of the LiDAR-driven actuator disk and turbulence closure, as well as a detailed outline of the calibration procedure. The novel approach is then verified (Sec. V), validated against real power data, and compared to other models of wind turbine wakes (Sec. VI). Finally, concluding remarks are discussed in Sec. VII.

II. CONCEPTUAL MODEL

Under steady conditions, negligible Coriolis and buoyancy forces, the flow around wind turbines can be described through the nondimensional RANS equations for incompressible turbulent flows,

$$\begin{cases}
\frac{\partial \bar{u}_{j}}{\partial x_{j}} = 0, \\
\bar{u}_{j} \frac{\partial \bar{u}_{i}}{\partial x_{j}} = -\frac{\partial \bar{p}}{\partial x_{i}} + \frac{1}{Re} \frac{\partial^{2} \bar{u}_{i}}{\partial x_{j} \partial x_{j}} - \frac{\partial \bar{u}'_{i} u'_{j}}{\partial x_{j}} + \bar{f}_{i},
\end{cases} (1)$$

and body force vector, respectively (\bar{f}_1 representing the turbine rotor thrust), and Re is the diameter-based Reynolds number. Within the present notation, repeated indices imply summation and bold quantities indicate vectorial quantities. The x_1 -axis (or x) is aligned with the turbine axis and points downstream, x_3 (or z) is the vertical direction, and x_2 (or y) is the traversal direction defined according to a righthanded reference system (Fig. 1). The velocity components in the (x, y, z) directions are (u, v, w), respectively. Throughout the paper, all the physical quantities have been made non-dimensional through the turbine diameter, D (length), incoming wind speed, U_{∞} (velocities), undisturbed dynamic pressure ρU_{∞}^2 , (pressure), and the purely dimensional terms $U_{\infty}D$ (eddy-viscosity), and $\rho U_{\infty}^2/D$ (forces per unit volume). It is noteworthy that utility-scale turbines operate within a range of Reynolds numbers $(Re^6 - Re^8)$ that justifies neglecting viscous terms in the wake modeling (i.e., the flow is *Re*-independent⁹⁵). The Boussinesq hypothesis allows expressing the deviatoric part

where $\bar{\mathbf{u}}$, \bar{p} , and $\bar{\mathbf{f}}$ are the Reynolds-averaged velocity vector, pressure,

of the Reynolds stress tensor to be proportional to the strain rate tensor through the turbulent eddy-viscosity, ν_T , as follows:

$$\overline{u_i'u_j'} = \frac{2}{3}\delta_{ij}\kappa - \nu_T \left(\frac{\partial \bar{u}_j}{\partial x_i} + \frac{\partial \bar{u}_i}{\partial x_j}\right),\tag{2}$$

where δ_{ij} is the Kronecker delta and κ the turbulent kinetic energy. By incorporating the first term on the RHS of Eq. (2) into a modified pressure, neglecting the molecular viscosity, and assuming a constant turbulent eddy viscosity, we obtain:

$$\begin{cases} \frac{\partial \bar{u}_{j}}{\partial x_{j}} = 0, \\ \bar{u}_{j} \frac{\partial \bar{u}_{i}}{\partial x_{i}} = -\frac{\partial \bar{p}}{\partial x_{i}} + \nu_{T} \frac{\partial^{2} \bar{u}_{i}}{\partial x_{i} \partial x_{i}} + \bar{f}_{i}, \end{cases}$$
(3)

where the Reynolds-stress term has been reduced by enforcing continuity.

For the P2D-RANS, the dimensionality of the problem is reduced from 3D to 2D by adopting a depth-averaged (or shallow water) approximation of the RANS equations, which requires the horizontal

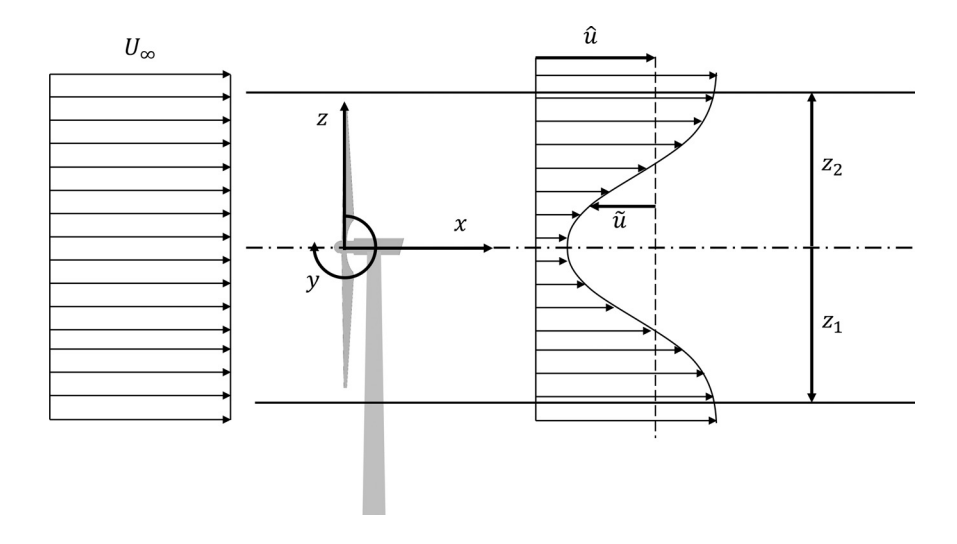


FIG. 1. Schematic of the reference system of the P2D-RANS and the shallow-water decomposition.

length and velocity scales of the mean flow to be significantly greater than their respective vertical quantities. For wind farm flows, this assumption may not be satisfied in the presence of significant vertical shear (which is at the moment not considered and can eventually be added *a posteriori* through a superposition model (73,80) or complex terrain, whose modeling is beyond the scope of this work.

We define a generic Reynolds-averaged scalar, $\bar{\xi}$, as the sum of a vertically averaged value, $\hat{\xi}$, and a *z*-varying (or dispersive) component, $\tilde{\xi}$, as sketched in Fig. 1. The depth-averaged parameter is defined as

$$\widehat{\xi}(x,y) = \frac{1}{z_2 - z_1} \int_{z_1}^{z_2} \overline{\xi}(x,y,z) dz,$$
(4)

where z_1 and z_2 are the vertical coordinates of the bottom and top boundaries, respectively, of the integration domain. In this work, these boundaries are selected as $z_2 = -z_1 = D/2$ to include the entire rotor layer, which is convenient to study wind turbines with uniform hub height and rotor diameter on flat terrain.

Application of the operator defined in Eq. (4) to both sides of Eq. (3) in conservative form, yields

$$\begin{cases}
\frac{\partial \widehat{u}}{\partial x} + \frac{\partial \widehat{v}}{\partial y} + \frac{\bar{w}_2 - \bar{w}_1}{z_2 - z_1} = 0, \\
\frac{\partial \widehat{u}}{\partial x} \widehat{u} + \frac{\partial \widehat{u}}{\partial y} \widehat{v} + \frac{\bar{u}_2 \bar{w}_2 - \bar{u}_1 \bar{w}_1 - \widehat{u}(\bar{w}_2 - \bar{w}_1)}{z_2 - z_1}
\end{cases}$$

$$= -\frac{\partial \widehat{p}}{\partial x} + \nu_T \left(\frac{\partial^2 \widehat{u}}{\partial x^2} + \frac{\partial^2 \widehat{u}}{\partial y^2} \right)$$

$$+ \widehat{f}_x + \frac{\nu_T}{z_2 - z_1} \left(\frac{\partial \bar{u}}{\partial z} \Big|_2 - \frac{\partial \bar{u}}{\partial z} \Big|_1 \right) - \frac{\partial \widehat{u} \widehat{u}}{\partial x} - \frac{\partial \widehat{u} \widehat{v}}{\partial y} \quad (5)$$

$$\frac{\partial \widehat{v}}{\partial x} \widehat{u} + \frac{\partial \widehat{v}}{\partial y} \widehat{v} + \frac{\bar{v}_2 \bar{w}_2 - \bar{v}_1 \bar{w}_1 - \widehat{v}(\bar{w}_2 - \bar{w}_1)}{z_2 - z_1}$$

$$= -\frac{\partial \widehat{p}}{\partial y} + \nu_T \left(\frac{\partial^2 \widehat{v}}{\partial x^2} + \frac{\partial^2 \widehat{v}}{\partial y^2} \right)$$

$$+ \widehat{f}_y + \frac{\nu_T}{z_2 - z_1} \left(\frac{\partial \bar{v}}{\partial z} \Big|_2 - \frac{\partial \bar{v}}{\partial z} \Big|_1 \right) - \frac{\partial \widehat{u} \widehat{v}}{\partial x} - \frac{\partial \widehat{v} \widehat{v}}{\partial y},$$

where subscript 1 and 2 refer to 3D quantities evaluated at z_1 and z_2 , respectively. Equation (5) include depth-averaged $(\hat{\ })$, 3D (-), and dispersive $(\tilde{\ })$ terms. While the first are explicitly solved by the P2D-RANS model, the last two contributions need to be modeled as a function of the depth-averaged field. By neglecting the wake swirling motion, which is only present in the near wake and has negligible effects on the streamwise velocity and power, and assuming an axisymmetric wake velocity field, which can be recovered for cases with no yaw misalignment of the turbine rotor by subtracting the incoming vertical profile of the incoming streamwise velocity, spanning the incoming to calculate these fluxes following the approach proposed by Boersma et al. Specifically, this allows defining linear operators that map the depth-averaged field (\hat{u}, \hat{v}) onto the corresponding axisymmetric streamwise velocity field (\bar{u}_x, \bar{u}_r) , as follows (see Appendix A for details):

$$\begin{cases} \bar{u}_x = M_u^{-1}(\widehat{u}), \\ \bar{u}_r = M_v^{-1}(\widehat{v}). \end{cases}$$
 (6)

Once the axisymmetric velocity components corresponding to a given provisional depth-averaged field are known, the vertical fluxes and the dispersive stresses in Eq. (5) can be numerically evaluated and fed as source terms into the model in an iterative way, as it will be detailed in Sec. III. In the case of side-wise multiple wake interaction, which causes a breakdown of the assumption of axisymmetric flow, an appropriate superposition of the single-wake vertical and dispersive fluxes is performed, as it will be described in Sec. V.

III. COMPUTATIONAL MODEL

The depth-averaged RANS equations (3) are solved in terms of velocity components using a marching scheme approach in the streamwise direction, *x*, while the pressure field is calculated iteratively due to its inherently elliptic nature. Problems where the streamwise diffusion is negligible but the pressure gradient is not are referred to as Partially Parabolized Navier–Stokes (PPNS)¹⁰² and provide advantages in terms of computational cost and data usage compared to fully elliptic solvers.¹⁰³ An essential feature of PPNS algorithms is the implementation of a pressure correction necessary to calculate the pressure field and enforce continuity to guarantee a divergence-free velocity field.

The PPNS scheme adopted for the P2D-RANS is inspired by previous works for ducted flows, 103–106 with the main difference that no velocity correction is enforced throughout the sweeps. The global pressure field is indeed corrected at the end of each parabolic sweep. The provisional velocity field does not satisfy mass conservation until the pressure correction achieves convergence (see Fig. 2).

The numerical scheme adopted for the momentum equations is identical to that documented in Ref. 107, except for the inclusion of the streamwise turbulent diffusion terms in Eq. (5), which are retained to enhance accuracy and numerical stability. The scheme is fully implicit, and the non-linear terms are treated via the lagging coefficient technique. ¹⁰² The uniform grid is staggered so that each velocity node is placed between two pressure nodes (Fig. 3). The momentum equations in their discretized form are:

$$\begin{cases} \widehat{u}_{i,j} \frac{\widehat{u}_{i+1,j} - \widehat{u}_{i,j}}{\Delta x} + \widehat{v}_{i+1,j} \frac{\widehat{u}_{i+1,j} - \widehat{u}_{i+1,j-1}}{2\Delta y} + \widehat{v}_{i+1,j+1} \frac{\widehat{u}_{i+1,j+1} - \widehat{u}_{i+1,j}}{2\Delta y} \\ = \frac{\widehat{p}_{i+1,j} - \widehat{p}_{i+2,j}}{\Delta x} + \nu_T \frac{\widehat{u}_{i+2,j} - 2\widehat{u}_{i+1,j} + \widehat{u}_{i,j}}{\Delta x^2} \\ + \nu_T \frac{\widehat{u}_{i+1,j+1} - 2\widehat{u}_{i+1,j} + \widehat{u}_{i+1,j-1}}{\Delta y^2} + \widehat{f}_{x,i+1,j}, \\ \widehat{\frac{u}_{i,j} + \widehat{u}_{i,j-1} \widehat{v}_{i+1,j} - \widehat{v}_{i,j}}{2\Delta x} + \widehat{v}_{i,j} \frac{\widehat{v}_{i+1,j+1} - \widehat{v}_{i+1,j-1}}{2\Delta y} \\ = \frac{\widehat{p}_{i+1,j-1} - \widehat{p}_{i+1,j}}{\Delta y} + \nu_T \frac{\widehat{v}_{i+2,j} - 2\widehat{v}_{i+1,j} + \widehat{v}_{i,j}}{\Delta x^2} \\ + \nu_T \frac{\widehat{v}_{i+1,j+1} - 2\widehat{v}_{i+1,j} + \widehat{v}_{i+1,j-1}}{\Delta y^2} + \widehat{f}_{y,i+1,j}, \end{cases}$$

where the indices i and j refer to the ith streamwise and jth spanwise locations, respectively. It is noteworthy that the 3D correction terms are tacitly included in the volumetric forces \hat{f} . The elliptic terms $\hat{u}_{i+2,j}, \hat{v}_{i+2,j}, \hat{p}_{i+2,j}$ are evaluated from the previous sweep. As indicated in Fig. 2, Eq. (7) is solved parabolically marching from the inlet to the outlet and twice for each sweep, first without streamwise diffusion and then with the streamwise diffusion activated.

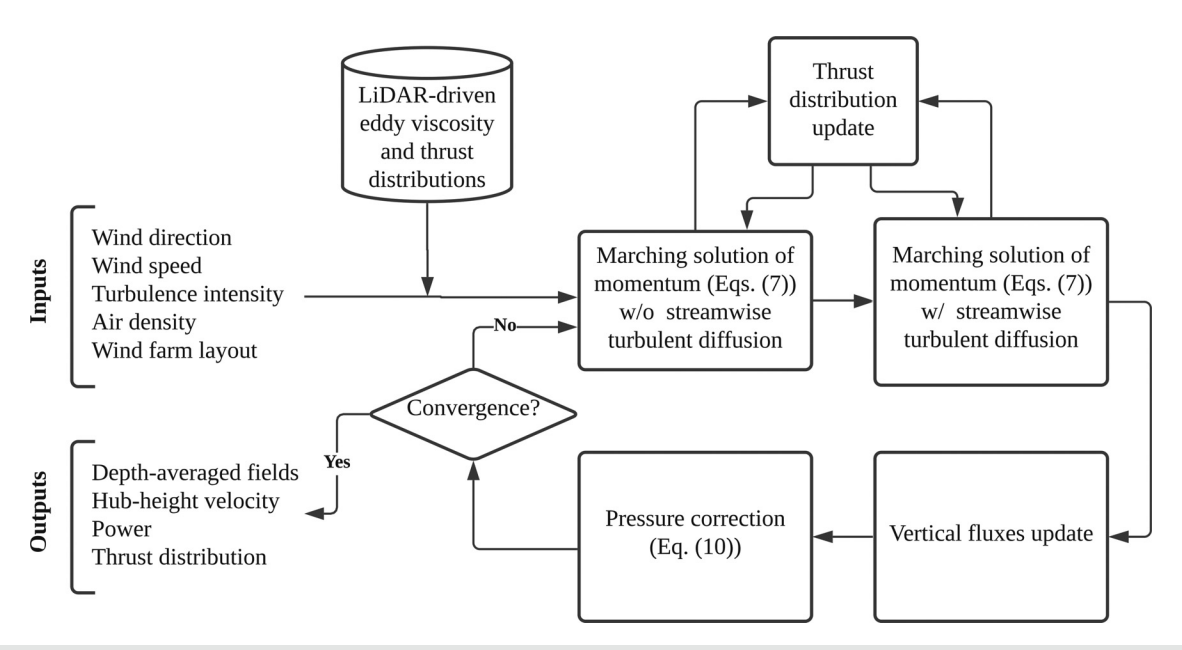


FIG. 2. Workflow of the P2D-RANS

The pressure correction is derived from first principles in Appendix B. The final form of the Poisson equation for the calculation of the corrective pressure field, p^c , that is applied at the end of each sweep to correct the provisional velocity is

$$\frac{\partial^2 \widehat{p}^c}{\partial x^2} + \frac{\partial^2 \widehat{p}^c}{\partial y^2} = \widehat{u} \frac{\partial \nabla}{\partial x} + \widehat{v} \frac{\partial \nabla}{\partial y} - \nu_T \left(\frac{\partial^2 \nabla}{\partial x^2} + \frac{\partial^2 \nabla}{\partial y^2} \right), \tag{8}$$

or, more concisely:

$$\nabla^2 \widehat{p}^c = \frac{D\nabla}{Dt} - \nu_T \nabla^2 \nabla, \tag{9}$$

where ∇ is the divergence of the provisional velocity field, including the correction for vertical mass fluxes. From a numerical standpoint, the pressure correction is discretized as

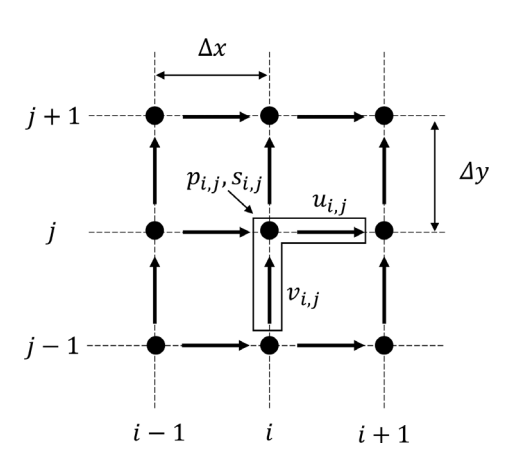


FIG. 3. Numerical grid of the P2D-RANS

$$\frac{\hat{p}_{i+1,j}^c - 2\hat{p}_{i,j}^c + \hat{p}_{i-1,j}^c}{\Delta x^2} + \frac{\hat{p}_{i,j+1}^c - 2\hat{p}_{i,j}^c + \hat{p}_{i,j-1}^c}{\Delta v^2} = s_{i,j}, \quad (10)$$

where

$$s_{i,j} = \widehat{u}_{i-1,j} \frac{\nabla_{i,j} - \nabla_{i-1,j}}{2\Delta x} + \widehat{u}_{i,j} \frac{\nabla_{i+1,j} - \nabla_{i,j}}{2\Delta x} + \widehat{v}_{i,j} \frac{\nabla_{i,j} - \nabla_{i,j-1}}{2\Delta y} + \widehat{v}_{i,j+1} \frac{\nabla_{i,j+1} - \nabla_{i,j}}{2\Delta y} - \nu_T \left(\frac{\nabla_{i+1,j} - 2\nabla_{i,j} + \nabla_{i-1,j}}{\Delta x^2} + \frac{\nabla_{i,j+1} - 2\nabla_{i,j} + \nabla_{i,j-1}}{\Delta y^2} \right),$$
(11)

and

$$\nabla_{i,j} = \frac{\widehat{u}_{i,j} - \widehat{u}_{i-1,j}}{\Delta x} + \frac{\widehat{v}_{i,j+1} - \widehat{v}_{i,j}}{\Delta y} + \frac{\overline{w}_{2,i,j} - \overline{w}_{1,i,j}}{z_2 - z_1},$$
(12)

where the last term represents the vertical mass flux obtained as explained in Sec. ${\rm II}$.

The Poisson equation for the pressure is solved through the *back-slash* Matlab solver for sparse linear systems. ¹⁰⁸ To speed up the convergence, the pressure correction is applied alternatively to all the cells and in blocks of 2×2 cells. ¹⁰⁹ Convergence is considered to be achieved when the mass residual, defined as the integral of the absolute value of the mass sources and sinks normalized by the incoming mass flow rate, is below 1%. ¹⁰⁷

Dirichlet boundary conditions on velocity $(\widehat{u}=1,\widehat{v}=0)$ and pressure $(\widehat{p}=0)$ are prescribed at the inlet and outlet, respectively. Non-homogeneous Neumann conditions are applied to the side boundaries by imposing the spanwise gradients of the velocity components to be equal to their respective values at the nearest y locations, which minimizes the backpropagation of boundary effects in the inner domain. Finally, a homogeneous Neumann boundary condition is

applied to the remaining boundaries for pressure, which is consistent with the Navier–Stokes equations. The spatial resolution of the grid is selected as $\Delta x=0.125$ and $\Delta y=0.05$, while the domain extends 15D away from the turbines in all directions. These parameters are selected after a comprehensive sensitivity analysis to ensure a mean percentage absolute error (MAPE) on the streamwise component smaller than 0.1% in the induction zone and 1% in the wake region. Figure 4 shows the results of the sensitivity analysis for an incoming wind speed set to $U_{\infty}=10\,\mathrm{m\,s^{-1}}$ and different levels of the incoming turbulence intensity, TI_{∞} .

IV. MODEL CALIBRATION

A. Experimental dataset

To enhance accuracy in predictions of the intra-wind-farm velocity field and wind turbine power capture, the P2D-RANS has been developed by encompassing a fully data-driven actuator disk model and turbulence closure, both calibrated through wind LiDAR measurements of individual wakes generated by utility-scale wind turbines. The onshore wind farm under examination is located in North Texas and includes 25 2.3-MW turbines of the same model, with a rotor diameter D = 108 m and hub height H = 80 m (Fig. 5).

A meteorological (met) mast is located at the South-East corner of the farm and recorded for the whole duration of the field campaign mean and standard deviation of horizontal wind speed and direction at 36, 60, and 80-m heights, barometric pressure at 2 and 75-m heights, and temperature at 3-m and 75-m heights. Furthermore, SCADA data in the form of mean and standard deviation of hubheight wind speed, active power, and other operational parameters were collected.

A WindCube 200S scanning pulsed Doppler wind LiDAR was deployed at the center of the farm from August 2015 to March 2017. This section provides a concise overview of the field campaign, since a detailed description of the site, experimental strategy, and LiDAR data processing can be found in previous related publications. ^{7,15,110}

The wind LiDAR was set up with a range gate of 50 m and an accumulation time of 500 ms. The scanning wind LiDAR performed Plan Position Indicator (PPI) scans with low elevation angles (typically 3°), azimuthal range of 20°, and rotation speed of the scanning head

of 2° s⁻¹, leading to a typical scanning time for a single PPI scan of 10 s. PPI scans were performed for wind directions included within the sector 145° – 235° when the wakes of turbines 1–6 are advected toward the LiDAR location. Overall, 16 765 quality-controlled PPI scans are available for the present study.

Individual LiDAR samples undergo a quality control process, including data rejection based on the dynamic filtering. ¹¹¹ After realigning the wake according to the 10-min-averaged wind direction, the horizontal equivalent velocity field, $u_{\rm eq}$, is made non-dimensional through the 10-min-averaged incoming vertical wind profile, according to the procedure outlined in Zhan *et al.* ¹⁵ Finally, the LiDAR measurements are reported in an axisymmetric-equivalent reference frame (x, r), where the radial position, r, represents the distance from the expected wake center. ¹⁵ The re-aligned and non-dimensional horizontal-equivalent wake velocity data are clustered in bins based on operative conditions (i.e., aerodynamic rotor thrust) and incoming wind turbulence intensity. The selection of the bin edges is guided by a preliminary characterization of the wind farm performance as a function of the inflow conditions, which is the object of Sec. IV B.

B. Wind turbine and wind farm performance

The operation of a pitch-regulated turbine can be characterized as a function of the hub-height density-corrected wind speed, 112 as follows:

$$U_{\text{norm}} = \frac{U_{\text{hub}}}{U_{\text{rated}}} \left(\frac{\rho}{\rho_0}\right)^{1/3},\tag{13}$$

where $U_{\rm hub}$ is the 10-min-averaged horizontal wind speed at hub height, $U_{\rm rated}=11~{\rm m~s}^{-1}$ is the rated wind speed, ρ is the measured air density, and $\rho_0=1.225~{\rm kg~m}^{-3}$ is the reference air density. Wake turbulent mixing and recovery can be conveniently investigated through the turbulence intensity, TI, defined as the ratio between the standard deviation of the hub-height wind speed over the mean of the same quantity. Specifically, Zhan *et al*^{1.5} identified through an atmospheric stability analysis values of 7% and 13.5% as thresholds of the incoming-wind turbulence intensity bounding stable (TI $_{\infty}<7\%$), near-neutral (TI $_{\infty}\in[7,13.5)\%$), and convective (unstable) (TI $_{\infty}\geq13.5\%$) regimes

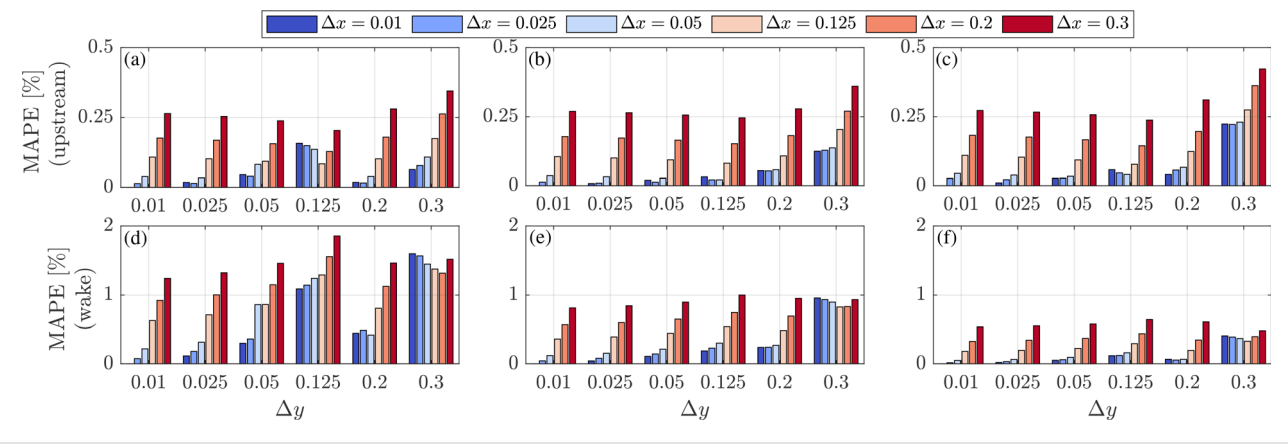


FIG. 4. Mean absolute percentage error with respect to the finest grid ($\Delta x = \Delta y = 0.01$) and for $U_{\infty} = 10 \text{ m s}^{-1}$: (a)–(c) induction zone (-5 < x < 0, |y| < 1); (d)–(f): wake region (0 < x < 15, |y| < 1); (a) and (d) $\text{TI}_{\infty} < 7\%$, (b) and (e) $\text{TI}_{\infty} \in [7, 13.5)\%$, and (c) and (f) $\text{TI}_{\infty} \ge 13.5\%$.

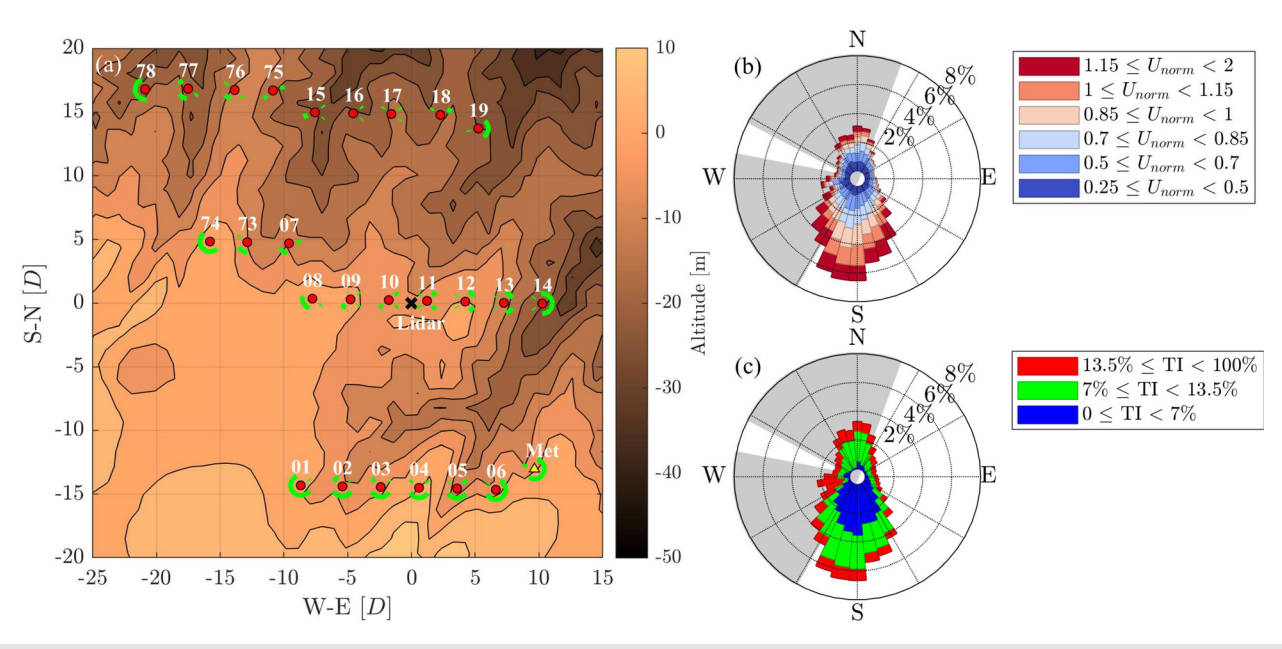


FIG. 5. Characterization of the wind farm under investigation: (a) topographic map of the site; (b) directional histogram of the normalized wind speed at hub height [Eq. (13)]; and (c) directional histogram of the incoming turbulence intensity at hub height. The green sectors in (a) represent the unwaked wind sectors, while the gray ones in (b) and (c) correspond to wind sectors where the met mast is likely affected by turbine wakes.

for the site under investigation. In general, the subscript ∞ refers to quantities recorded by the SCADA not affected by wakes and is, thus, representative of the incoming wind field. In this work, wind sectors affected by wakes are defined according to the 61400–12, Annex B of the IEC standards. ¹¹³

Wind speed at hub height, $U_{\rm hub}$, is retrieved based on the measurements of the nacelle anemometer, which undergoes quality control and correction processes. First, occurrences of unrealistic velocity and turbulence intensity, extreme veer, yaw misalignment, idling sensors, and zero or negative active power are rejected (see Table I). Then the nacelle transfer function is calculated based on met-tower normalized wind speed collected at 80-m height and the nacelle anemometer of Turbine 06 (namely, the closest turbine to the met tower) only for unwaked wind sectors, in compliance with the International IEC Standards. 113 Such transfer function cannot be applied directly to the

TABLE I. Breakdown of the quality check on meteorological and SCADA data.

	Formulation	Rejection rate (%)	
Veer	$\frac{d\theta_w}{dz} > 0.25^{\circ} \text{ m}^{-1}$	16.3	
Idling wind direction	$\frac{d\theta_w}{dt} = 0$ $ \theta_{\text{yaw}} - \theta_w > 30^{\circ}$	2.1	
Yaw misalignment	$ \theta_{\rm yaw} - \theta_w > 30^\circ$	1.6	
Idling power	$\frac{dP_{\text{norm}}}{dt} = 0$	0.04	
No power	$P_{ m norm} \leq 0$	9.9	
Zero velocity	$U_{ m norm}=0$	0.02	
Off-range TI	$TI \le 0 \text{ or } TI > 100\%$	1.1	

whole park since biases of up to 5% between different SCADA anemometers are present. The mentioned biases are estimated by comparing the raw individual power curves. ¹¹ Therefore, all the wind speed data are re-scaled by a multiplicative factor using the data of Turbine 06 as a reference before the correction for the nacelle flow distortion.

The experimental turbine power curve is calculated by leveraging the data from all the turbines following the IEC Standards. 113 To flag power curtailments associated with off-design operations, an initial nominal power curve is generated based on the power of reference Turbine 06 only and the met-tower normalized wind speed only for unwaked sectors. Power reads exhibiting a deficit larger than 300 kW from the power estimated through the nominal power curve (\sim 1% of the cases) are then rejected. 114 The final power curves are generated using all the available SCADA data (August 2015-April 2017) and differentiated as a function of TI. 115 It is noteworthy that power in region III can exceed the nameplate value by virtue of the power-boost mode, which enables the generator to produce additional power under favorable operative conditions. The TI-based normalized power (P_{norm}) curves are reported in Fig. 6(a). The accuracy of this method is assessed quantitatively by evaluating the error between the measured power and the power obtained from the different power curves and using either met or SCADA (corrected) hub-height wind speeds as input variables. The error metric used here is the normalized mean absolute error, 49 which is defined as

$$NMAE(x, x_{ref}) = \frac{\sum_{i} |x_i - x_{i,ref}|}{\sum_{i} x_{i,ref}},$$
(14)

where x and x_{ref} represent the modeled and reference value of the target quantity, respectively. This error analysis indicates that the best

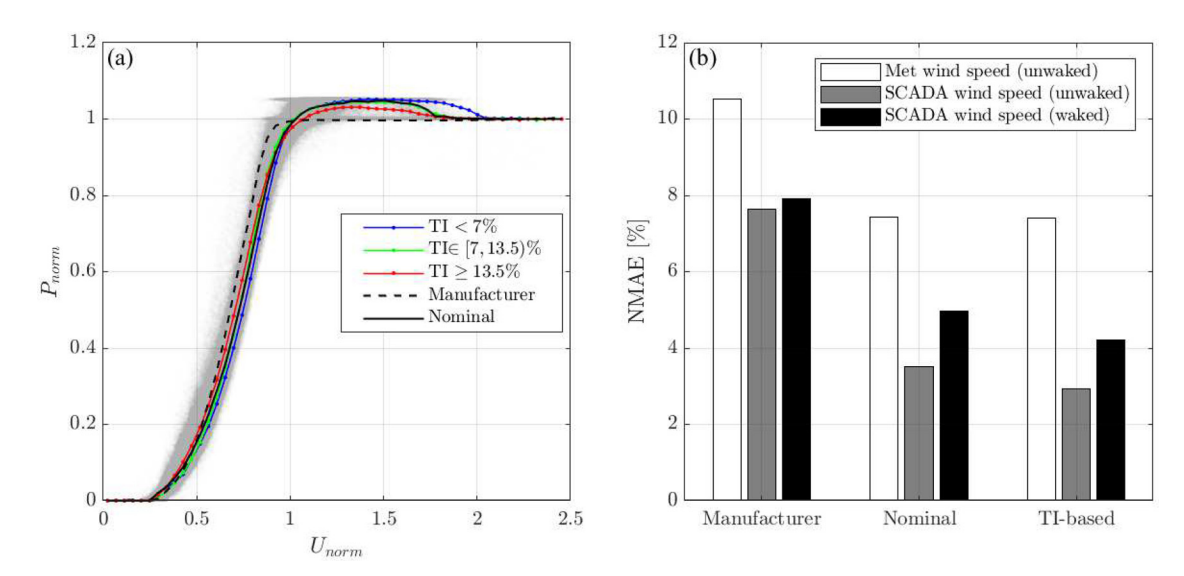


FIG. 6. (a) Power curves for different stability classes. The gray dots represent quality-controlled 10-min-averaged data. (b) Normalized Mean Absolute Error (NMAE) of the SCADA 10-min-averaged power and the power obtained through different power curves and using different inputs as in incoming wind speed.

agreement with the SCADA data is achieved by using the TI-based power curves and the corrected SCADA wind speed as input. Slightly worse accuracy is obtained by using the nominal power curve. The highest error associated with the met tower wind speed is due to the presence of spatial heterogeneity of the flow over the farm. ¹¹⁴ Further, higher uncertainty is observed for the power output of waked turbines, likely due to the more heterogeneous velocity distribution over the rotor area not captured by the nacelle anemometer.

Similar procedures are used to evaluate the power coefficient, c_p , and total farm power curve, which guide the selection of the bin edges of the incoming normalized hub-height velocity, $U_{\text{norm},\infty}$, used for the clustering of the LiDAR data. The heat map of Fig. 7(a) shows the occurrence of $[U_{\text{norm},\infty}, \text{ TI}_{\infty}]$ pairs based on the available SCADA data for unwaked turbine operations. The green dots refer to the SCADA data paired with the LiDAR scans, which can be seen to cover satisfactorily most of the typical wind conditions, except for the $U_{\text{norm},\infty} < 0.5$, $\text{TI}_{\infty} < 13.5\%$ region. For this study, bin edges in

 $U_{\mathrm{norm},\infty}$ are selected as [0.25,0.5,0.7,0.85,1,1.15,2] [see Fig. 7(b)] and are purposely refined in the proximity of the turbine rated power (i.e., $U_{\mathrm{norm},\infty}=1$), where a stronger variation of c_p and, thus, thrust coefficient, are expected. Finally, as highlighted by the farm power curve calculated including all the turbines regardless of their waked/ unwaked state [Fig. 7(c)], for $U_{\mathrm{norm},\infty}>1.15$, the average total farm power is practically equal to the nominal capacity of the wind plant. The numerical modeling of such cases is irrelevant for the assessment of the proposed wind farm model in terms of power capture, and further bins for very high $U_{\mathrm{norm},\infty}$ are thus not defined. Table II reports the number of raw and quality-controlled experimental LiDAR samples available for each cluster.

C. Data-driven calibration of the RANS model

The mean streamwise velocity for each cluster is reconstructed using the LiDAR Statistical Barnes Objective Analysis (LiSBOA)

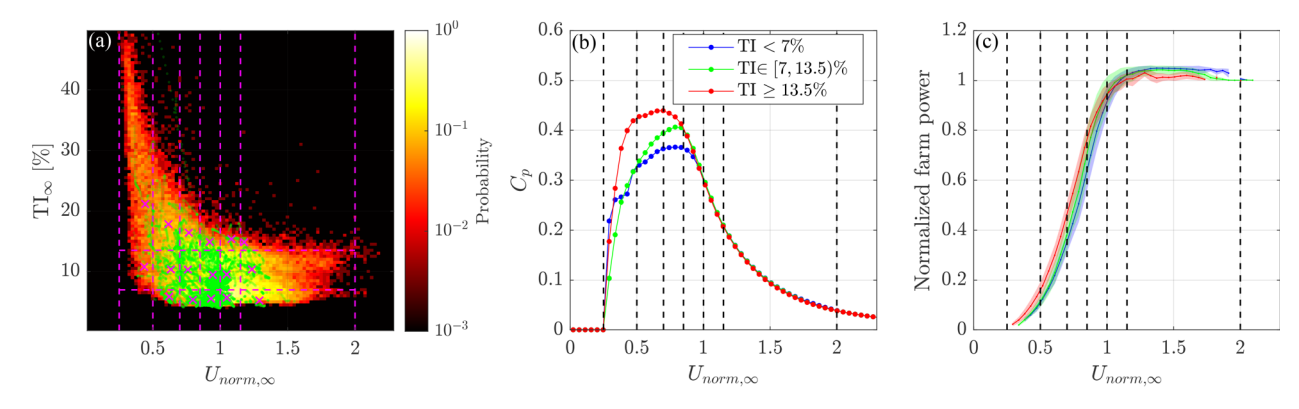


FIG. 7. Selection of the bin edges: (a) two-dimensional pdf of $U_{\text{norm},\infty}$ and TI_{∞} (green dots correspond to available LiDAR scans, while crosses indicate the bin centroids); (b) average c_p experimental curves; and (c) overall normalized farm power as a function of $U_{\text{norm},\infty}$, where the shaded areas represent standard deviation. The dashed lines separate the different bins in $U_{\text{norm},\infty}$.

TABLE II. Number (in millions) and percentage (in brackets) of quality-controlled LiDAR samples available for each cluster.

	TI $_{\infty} < 7\%$	TI $_{\infty}\in[7,13.5)\%$	TI $_{\infty} \geq$ 13.5%
$U_{\text{norm},\infty} \in [0, 0.25)$	0	0.04 (0.3)	0.24 (1.8)
$U_{\text{norm},\infty} \in [0.5, 0.7)$	0.29 (2.2)	0.88 (6.6)	0.52 (3.9)
$U_{\text{norm},\infty} \in [0.7, 0.85)$	0.77 (5.8)	1.32 (9.9)	0.42 (3.1)
$U_{\mathrm{norm},\infty} \in [0.85,1)$	1.77 (20.7)	2.87 (21.5)	0.3 (2.2)
$U_{\text{norm},\infty} \in [1, 1.15)$	0.58 (4.4)	1.46 (11.0)	0.16 (1.2)
$U_{\mathrm{norm},\infty} \in [1.15,2)$	0.21 (1.6)	0.48 (3.6)	0.03 (0.2)

tool 116,117 on a Cartesian grid with fundamental half-wavelengths $\Delta n_{0,x}=1.5D, \Delta n_{0,r}=0.5D$ and region with local data spacing $\Delta \tilde{d}>0.25$ are rejected (refer to Ref. 116 for more theoretical details on LiSBOA). Data voids are filled through a bi-harmonic interpolation algorithm. The velocity fields in axisymmetric coordinate are finally

depth-averaged to build the reference dataset of $\widehat{u}(x,y,U_{\text{norm},\infty},\text{TI}_\infty)$, which are reported in Fig. 8. Results are not shown for two bins, which fail to satisfy the statistical constraints imposed by the LiSBOA due to the limited availability of data points. The used methodology for the characterization of the wake velocity field captures satisfactorily the reduced velocity deficit occurring for cases with lower c_t (i.e., for $U_{\text{norm},\infty} \gtrsim 0.85$), as well as the faster wake recovery occurring with increasing turbulence intensity. The quantification of the wake variability with incoming wind speed and turbulence intensity is instrumental for the calibration of the actuator disk and the turbulence closure model of the P2D-RANS and, more in general, for accurate modeling of the wind farm flow.

The tuning of the turbulent eddy-viscosity and axial force distribution are performed following the methodology introduced by Iungo *et al.*, ⁹⁰ but adopting depth-averaged velocity fields and the P2D-RANS model instead of the axisymmetric flow and RANS model of the original publication. The present calibration procedure includes the following steps:

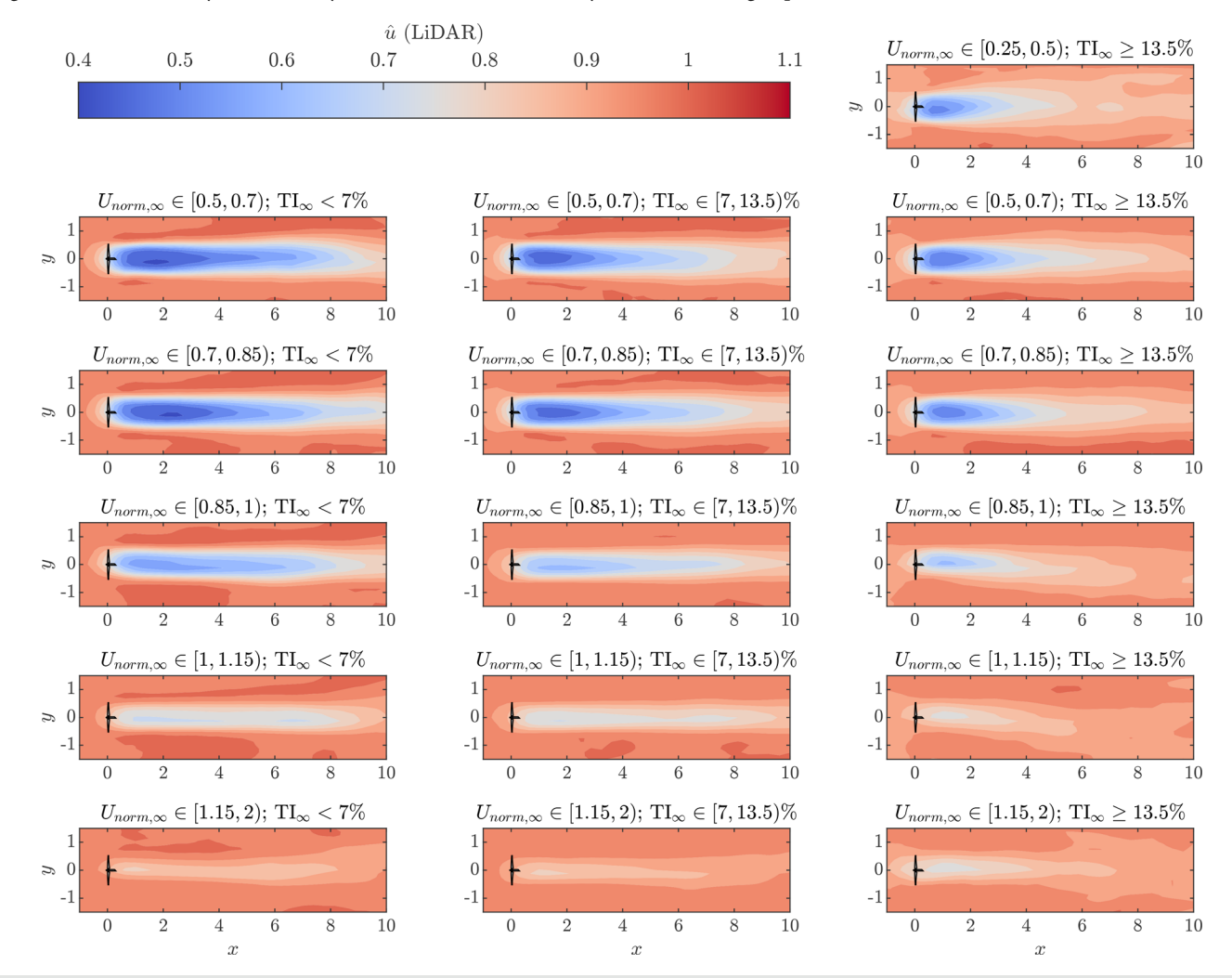


FIG. 8. Mean streamwise, depth-averaged velocity fields (\widehat{u}) calculated from the LiDAR data for the various bins defined based on hub-height wind speed, $U_{\text{norm},\infty}$, and, turbulence intensity, Tl_{∞} .

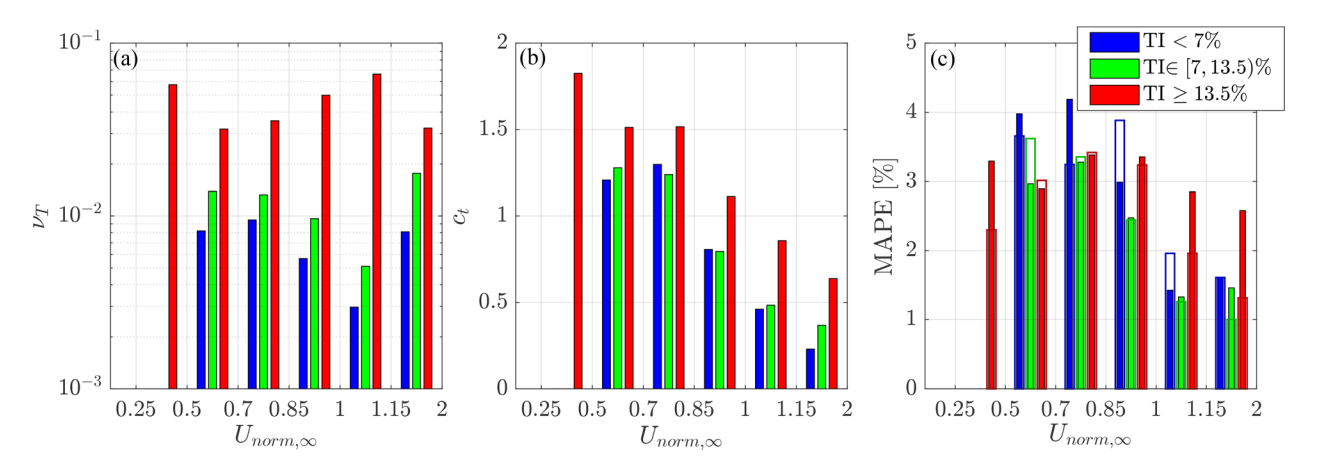


FIG. 9. Calibration of the P2D-RANS: (a) optimal turbulent eddy-viscosity; (b) optimal thrust coefficient, c_i ; and (c) mean absolute percentage error (MAPE) (empty bars represent the MAPE for the far wake velocity field after the optimization of ν_T only, and the full ones represent the final MAPE after the estimation of the axial load).

- the near wake length, x_{NW} , namely the extension of the region where the pressure gradients are relevant, is estimated as the streamwise location where the minimum rotor-averaged velocity occurs: 119
- a constant turbulent eddy-viscosity is estimated by minimizing the MAPE between the average streamwise wake velocity predicted with the P2D-RANS and that obtained from the LiDAR data, where:

$$MAPE = \left\langle \frac{|\widehat{u}_{P2D-RANS}(x, |y| < 1) - \widehat{u}_{LiDAR}(x, |y| < 1)|}{\widehat{u}_{LiDAR}(x, |y| < 1)} \right\rangle, \quad (15)$$

with $\langle \rangle$ indicating space average. In this case, the modified P2D-RANS solver does not include the rotor region, instead the \widehat{u} velocity profile calculated from the LiDAR data at $x_{\rm NW}$ is injected as inlet boundary condition, while assuming constant pressure to calculate \widehat{v} . The optimization algorithm used to estimate turbulent eddy-viscosity is described in Iungo $et\ al.$; ⁹⁰

 once the optimal ν_T is known, the axial thrust force on the turbine rotor is estimated by correcting iteratively the streamwise forcing, \widehat{f}_x , in the full version of the P2D-RANS model to match the experimental velocity profile at x_{NW} as:

$$\int_{-\infty}^{+\infty} \widehat{f_x}^{n+1}(x,y) dx = \int_{-\infty}^{+\infty} \widehat{f_x}^{n}(x,y) dx + \widehat{u}_{P2D-RANS}(x_{NW},y)^2 - \widehat{u}_{LiDAR}(x_{NW},y)^2,$$
(16)

where the index n is the iteration counter. This method represents a simplified version of the technique based on the local momentum budget. ⁹⁰ It is noteworthy that the integrals in the x-direction are included only to compensate for the streamwise smoothing of the forces applied in the P2D-RANS to prevent numerical instabilities (further details of the formulation of the aerodynamic loads are provided in Appendix C). The algorithm stops when variation in the above-defined MAPE lower than 0.1% is attained (generally with less than 5–6 iterations).

The results of the calibration procedure are summarized in Figs. 9 and 10. The behavior of the optimal turbulent eddy-viscosity [Fig. 9(a)] lends interesting insight into the wake recovery process. The most consistent pattern is the increase in ν_T as a function of TI_{∞} ,

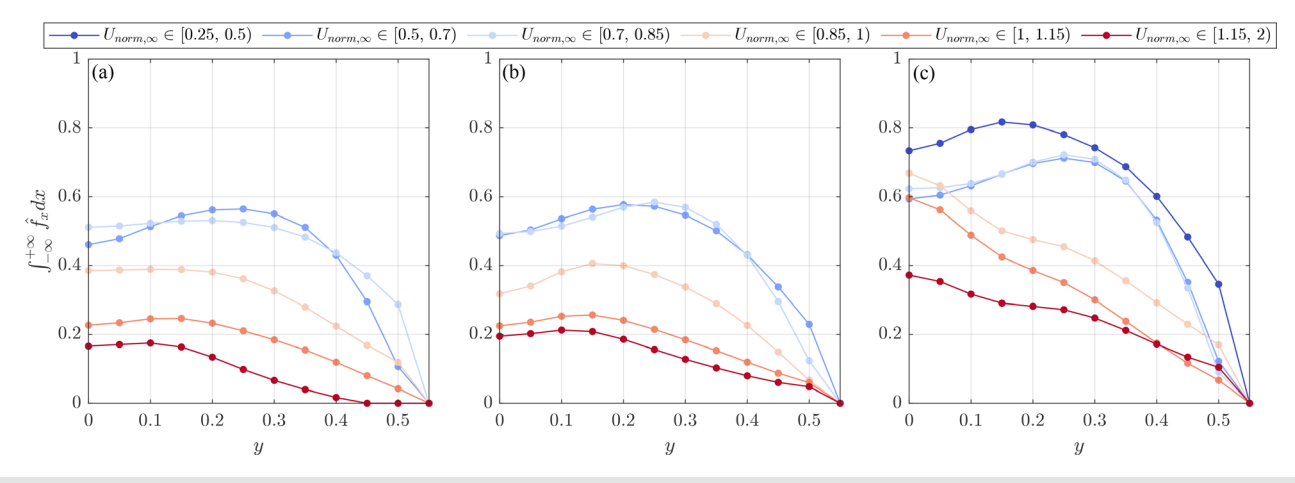


FIG. 10. Optimal axial forcing distribution after calibration: (a) TI $_{\infty}$ < 7%; (b) TI $_{\infty}$ \in [7, 13.5)%; and (c) TI $_{\infty}$ \geq 13.5%.

which is expected since TI_∞ is linked to the magnitude of the turbulent momentum fluxes in the wake. The turbulent eddy viscosity increases by nearly tenfold in convective conditions compared to stable conditions, which confirms the necessity of including effects of atmospheric stability in wind farm models. Furthermore, the turbulent eddy-viscosity for low and moderate TI_∞ decreases as a function of $U_{\mathrm{norm},\infty}$, except for the last bin $U_{\mathrm{norm},\infty} \in [1.15,2)$. Our interpretation is that the ν_T optimizer identifies effects related to the wake-added turbulence, which is indeed stronger for higher c_t value (i.e., low $U_{\mathrm{norm},\infty}$) conditions due to the enhanced shear-generated turbulence. The proportionality of the turbulent eddy viscosity to the velocity deficit, Δu , (i.e., c_t), is predicted by the shear flow theory, which produces the well-known scaling $\nu_T \sim r_w \Delta u$, where r_w is the wake radius, for a self-similar axisymmetric wake.

It is noteworthy that ν_T for convective conditions increases between $U_{\text{norm},\infty} = 0.5$ and 1.15. This trend, which is reversed compared to what is observed for low to moderate incoming TI_\infty conditions, is likely due to a different wake recovery mechanism occurring for unstable atmospheric conditions, where the incoming turbulence significantly contributes to the momentum diffusion in the wake, especially through the flow dynamics connected with wake meandering. Furthermore, the inverse proportionality between ν_T and c_t observed in convective conditions may be due to the damping of the largest incoming coherent structures operated by the rotor already documented by Chamorro et al., 120 which is expected to be more severe for high c_t . A more thorough investigation of this interesting behavior will be the object of future work. Finally, the reduction of ν_T observed for the last bin $U_{\text{norm},\infty} \in [1.15, 2)$ is ascribed to the very shallow wake deficit, which makes the definition of an eddy viscosity quite elusive. It is important to reiterate that, in this context, TI_{∞} represents a convenient engineering parameter associated with the velocity fluctuations connected with the shear and buoyancy generated turbulence, while a more comprehensive characterization of the incoming wind field should encompass the quantification of a reference turbulence length scale and the atmospheric stability regime, e.g., through the Obukhov length or the Richardson number.

Figures 9(b) and 10 show c_t and the spanwise distribution of depth-averaged thrust force. The thrust coefficient is practically constant for $0.25 \le U_{\text{norm},\infty} < 0.7$ (i.e., region II of the power curve), and then it decreases due to the blade pitching and tipspeed ratio reduction operated by the controller to limit the power output to the nameplate capacity. The only available thrust-force profile at very low $U_{\text{norm},\infty}$ corresponds to convective conditions, which shows an overall higher aerodynamic force. The force distribution is less sensitive to the atmospheric stability, although slightly higher values are estimated in high TI conditions. 90 Figure 9(c) shows a MAPE that lies below the 5% threshold for all the wakes after the calibration, which is considered satisfactory. To conclude, the calibrated numerical fields are shown in Fig. 11, while the difference fields (P2D-RANS minus LiDAR) are reported in Fig. 12. Finally, Tables III and IV provide ν_T and c_t resulting from the calibration procedure.

For the implementation of the P2D-RANS, the values of the calibrated rotor thrust coefficient and turbulent eddy-viscosity are assigned to the bin centroids displayed in Fig. 7(a) and investigated through a linear/nearest-neighbor Delauney interpolation to perform simulations with an arbitrary inflow.

V. VERIFICATION

According to the technical report AIAA, 121 the process of determining if a model implementation accurately represents the conceptual description and the solution of a model is referred to as verification. The purpose of this section is indeed to verify the validity of the proposed shallow-water approach corrected for vertical fluxes and dispersive terms, the pressure correction algorithm of the P2D-RANS, and the numerical method. To this aim, the P2D-RANS solution of a single-wake velocity field is compared to the equivalent result calculated through an elliptic axisymmetric RANS solver. The latter uses the Newton algorithm to solve the full non-linear set of RANS equations in cylindrical coordinates discretized through a spectral collocation method based on Chebyshev polynomials (for more details, refer to Refs. 90 and 122, while the code is publicly available 123) The simulations with the axisymmetric code are carried out using equivalent boundary conditions, turbine load, and turbulence model. The inflow conditions are arbitrarily chosen as $U_{\infty} = 10 \,\mathrm{m\,s}^{-1}$, $TI_{\infty}=10\%$, which in turn define the axial aerodynamic thrust and the turbulent eddy viscosity (Sec. IV).

Figure 13 shows the spanwise profiles of $\hat{u}, \hat{v}, \hat{p}$ extracted at several downstream locations calculated by the axisymmetric solver (dots) and the P2D-RANS (solid lines), as well as the same quantities for a purely 2D solver, i.e., without 3D corrections (dashed lines). The agreement between the axisymmetric solver (i.e., the benchmark) and the P2D-RANS is excellent, with negligible discrepancies, which are due to the slightly different implementation of the boundary conditions for the two models.⁹⁰ The almost perfect overlapping between the pressure obtained by the axisymmetric RANS solving the fully elliptic Navier-Stokes equations and through the iterative marching scheme of the P2D-RANS described in Sec. III serves as verification of the proposed pressure-velocity coupling scheme. Conversely, the profiles obtained with the merely 2D-RANS code exhibit significantly higher speedups, hampered wake recovery, excessive spanwise velocity magnitude, and pressure gradients compared to the benchmark simulations, which justifies the utilization of the proposed 3D corrections to relax the vertical confinement, which is a typical limitation of 2D wind farm flow simulators.

The 3D correction terms introduced in the P2D-RANS are assessed by plotting in Fig. 14 the individual contributions of the vertical fluxes and dispersive terms [overbarred and tilded terms, respectively, in Eq. (4)] to the mass (left column), *x*-momentum (center), and *y*-momentum (right) budgets. For an isolated turbine, these terms peak in the rotor area and drop sharply outside of the rotor span and decay further downstream as the wake recovers, and cross-stream components dissipate. The significance of the 3D corrective terms within the P2D-RANS equations is further explored in Fig. 15, where the individual terms constituting the mass and momentum balances are visualized separately. For the momentum equations, the vertical and dispersive fluxes are generally one order of magnitude smaller than the dominant terms (advection and pressure) in the rotor region, but become relatively significant in the far wake, which is dominated by turbulent diffusion.

It is noteworthy that the results of the present verification hold valid for an arbitrary turbine thrust and eddy viscosity, namely, for the full range of inflow conditions defined in the calibration phase (Sec. IV).

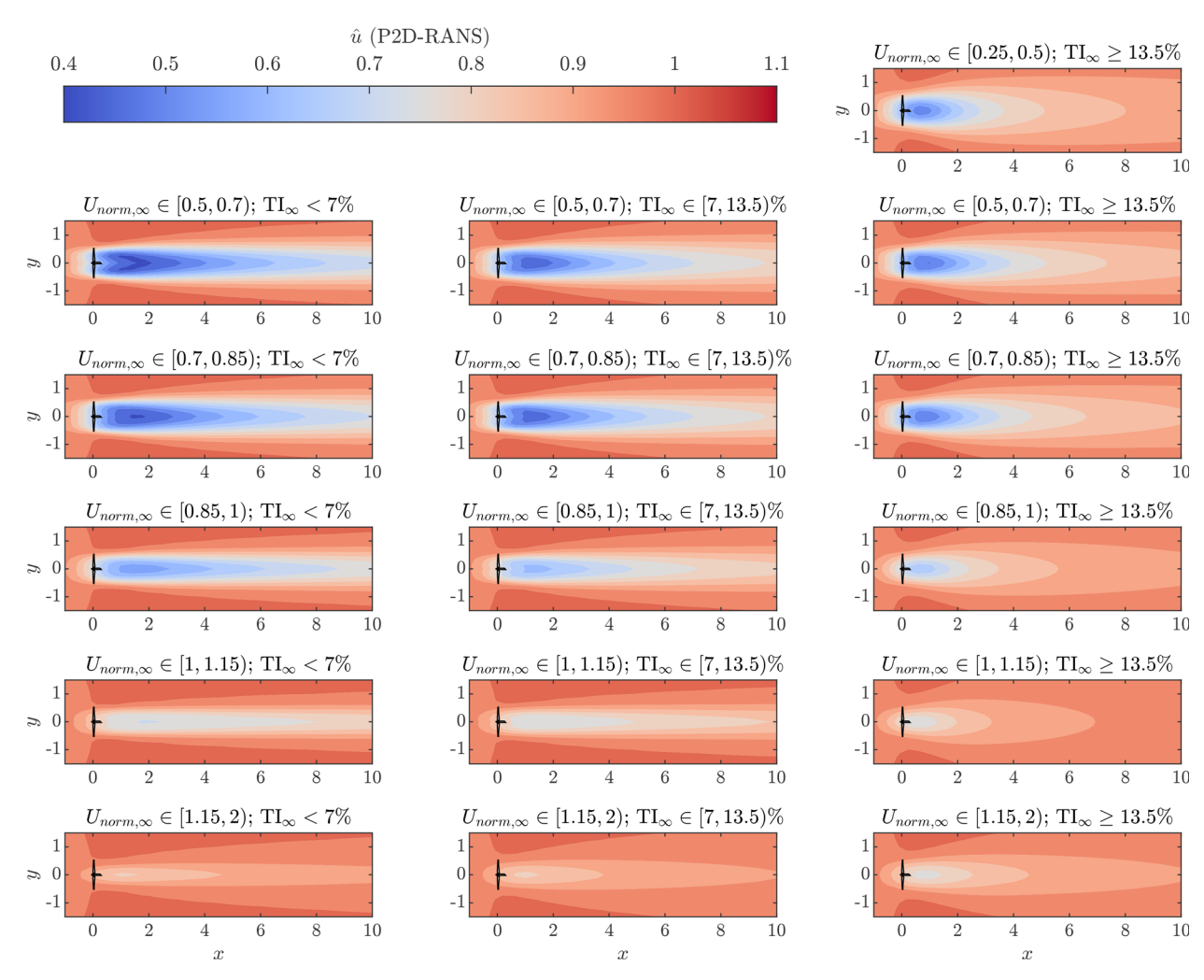


FIG. 11. Mean streamwise, depth-averaged velocity fields (\widehat{u}) of the P2D-RANS after calibration.

For the simulation of a wind farm flow, the assumption of axially symmetrical and non-swirling flow underpinning the method for the estimation of the 3D effects described in Appendix A fails due to the merging of multiple wakes. Therefore, it is necessary to formulate an appropriate superposition method of the vertical fluxes and dispersive terms of the single turbines. To this aim, the flow resulting from the interaction of two in-tandem turbines with a streamwise spacing of 5D is calculated through the axisymmetric elliptic RANS and the P2D-RANS. The latter estimates the overall vertical mass and momentum fluxes through a superposition of those obtained for single-wake simulations and stored in a lookup table as a function of $U_{\mathrm{norm},\infty}$ and TI_∞ and interrogated through a nearest-neighbor method. Namely, the 3D corrections are evaluated for 15 values of $U_{\text{norm},\infty}$ from 0.2 to 2 and 12 values of ${\rm TI}_{\infty}$ from 4% to 50% (i.e., 180 total single-wake cases), which cover the 98.5% of the climatology of the Panhandle wind farm. The domain considered for single-wake fluxes extends from -4D to 20Din the streamwise direction and $\pm 2D$ in the spanwise direction, since vertical fluxes and dispersive terms beyond such region are negligible

for a wide range of operative conditions (see Fig. 14). Different methods have been considered for the estimate of the total fluxes resulting from wake overlapping, such as linear sum, root-squared signed sum, and the maximum absolute value of the single-wake contributions. The error with respect to the axisymmetric RANS, which solves directly the full flow equations without any simplifying assumption, is quantified to identify the best performing superposition principle. A total of 18 simulations of two in-tandem wind turbines with 5D streamwise spacing are performed for each method, each one having as input the centroid of the clusters in terms of $U_{\text{norm},\infty}$ and TI_{∞} previously defined. This analysis aims to characterize the flow-dependent error for various wake conditions.

The MAPE of \widehat{u} for all the simulations is provided in Fig. 16 and indicates the root squared method with sign as that exhibiting the overall best agreement, with error exceeding 2% for only one case (stable, region II). It is noteworthy that the MAPE in \widehat{u} due to the superposition of the 3D corrections is always lower than 3%, which is quite smaller than the errors reported for traditional engineering wake

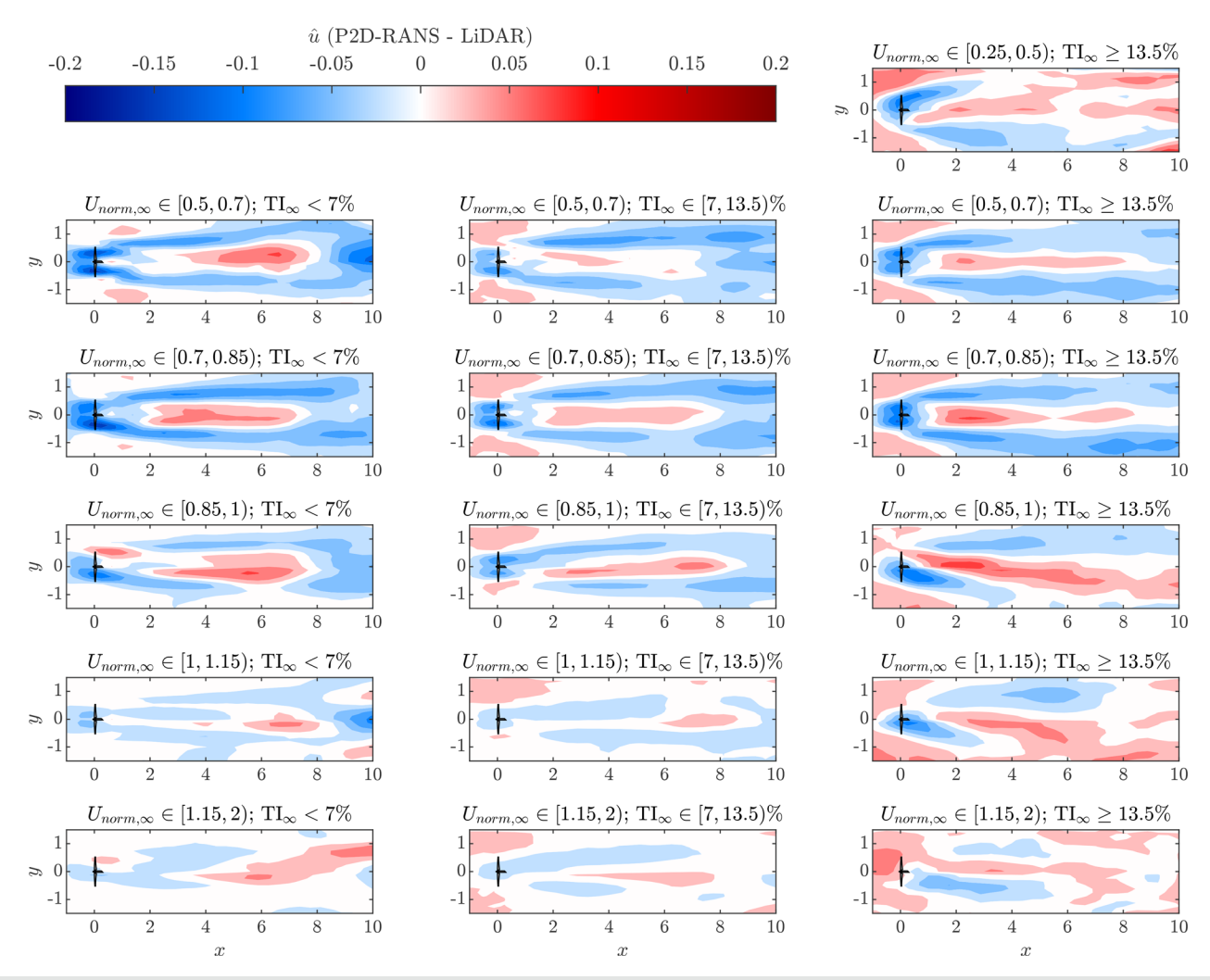


FIG. 12. Difference \widehat{u} velocity field between P2D-RANS and LiDAR after calibration.

models, for which these types of superposition methods are applied directly on the velocity field. $^{45,124}\,$

Figure 17 shows three selected cases with two in-tandem turbines with 5D streamwise spacing for the centroid of the cluster $U_{\text{norm},\infty}$ $\in (0.75, 0.8]$ (optimal c_t) and different TI_{∞} simulated through the

TABLE III. Optimal turbulent eddy viscosity of the P2D-RANS model. The value is made non-dimensional by $U_{\infty}D$.

	$TI_{\infty} < 7\%$	$TI_{\infty} \in [7,13.5)\%$	$TI_{\infty} \geq 13.5\%$
$U_{\mathrm{norm},\infty} \in [0, 0.25)$	N/A	N/A	0.0575
$U_{\mathrm{norm},\infty} \in [0.5, 0.7)$	0.0082	0.0139	0.0318
$U_{\mathrm{norm},\infty} \in [0.7, 0.85)$	0.0095	0.0133	0.0356
$U_{\mathrm{norm},\infty} \in [0.85,1)$	0.0057	0.0097	0.0499
$U_{\mathrm{norm},\infty} \in [1, 1.15)$	0.003	0.0051	0.0663
$U_{\mathrm{norm},\infty} \in [1.15,2)$	0.0081	0.0176	0.0323

reference elliptic RANS solver and the P2D-RANS with the root-squared signed sum method. The difference fields [Figs. 17(g)–17(i)] show that a systematic velocity underestimation takes place in the near wake region for the P2D-RANS, where vertical fluxes and dispersive terms peak, while the error decreases in magnitude and switches sign

TABLE IV. Coefficient of thrust calibrated on LiDAR data.

	$TI_{\infty} < 7\%$	$TI_{\infty} \in [7,13.5)\%$	$TI_{\infty} \geq 13.5\%$
$U_{\mathrm{norm},\infty} \in [0, 0.25)$	N/A	N/A	1.83
$U_{\mathrm{norm},\infty} \in [0.5, 0.7)$	1.21	1.28	1.51
$U_{\text{norm},\infty} \in [0.7, 0.85)$	1.3	1.24	1.52
$U_{\mathrm{norm},\infty} \in [0.85,1)$	0.81	0.8	1.11
$U_{\text{norm},\infty} \in [1, 1.15)$	0.46	0.48	0.86
$U_{\mathrm{norm},\infty} \in [1.15,2)$	0.23	0.37	0.64

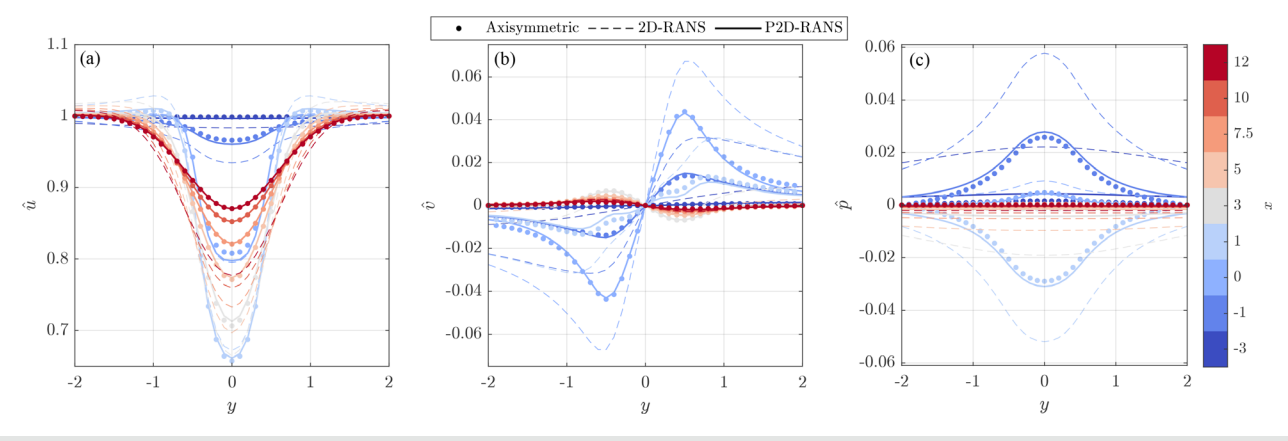


FIG. 13. Comparison between the depth-averaged fields of the elliptic axisymmetric RANS solver, a purely 2D-RANS code, and the P2D-RANS with 3D corrections: (a) streamwise velocity component; (b) spanwise velocity component; and (c) pressure.

moving downstream. These features are observed in most of the simulations performed for this analysis and indicate that the empirical superposition technique of the 3D corrections may lead to substantial errors only in the case of very close wake interaction (e.g., with streamwise spacing smaller than 3D), which is however unlikely for well-designed wind farms. A more in-depth investigation on the accuracy of the 3D corrections and the superposition method through a comparative analysis with a fully 3D RANS might be the object of future work.

VI. VALIDATION

The validation of a computational model is formally defined as "the process of determining the degree to which a model is an accurate representation of the real world from the perspective of the intended uses of the model." ¹²¹ In our case, real-world data are available in the form of 10-min-averaged power from the SCADA data of the wind farm under investigation. The applications of the P2D-RANS model, considering its potential in accuracy and computational costs, can be

broadly classified into two categories: (i) real-time diagnostic and control of wind turbines; and (ii) wind farm performance analysis and optimal design. The former focuses on the estimation of the time variability of power production (typically in the form of 10-min-averaged quantities) and accuracy of the P2D-RANS is assessed by comparing model predictions with the SCADA data for specific time series. The second application mainly entails the evaluation of wind turbine and wind farm performance in terms of power capture and quantification of wake losses as a function of atmospheric and turbine operational parameters. In this case, the following performance indicators are evaluated:

 percentage power losses,⁷ which are more relevant from the single-turbine modeling standpoint and are defined as follows:

$$\Delta P_i(t_j) = 1 - \frac{P_i(t_j)}{P_{\infty,i}(t_j)},\tag{17}$$

where $P_i(t_j)$ and $P_{\infty,i}(t_j)$ are the actual and unwaked power of the ith turbine at time t_i , respectively;

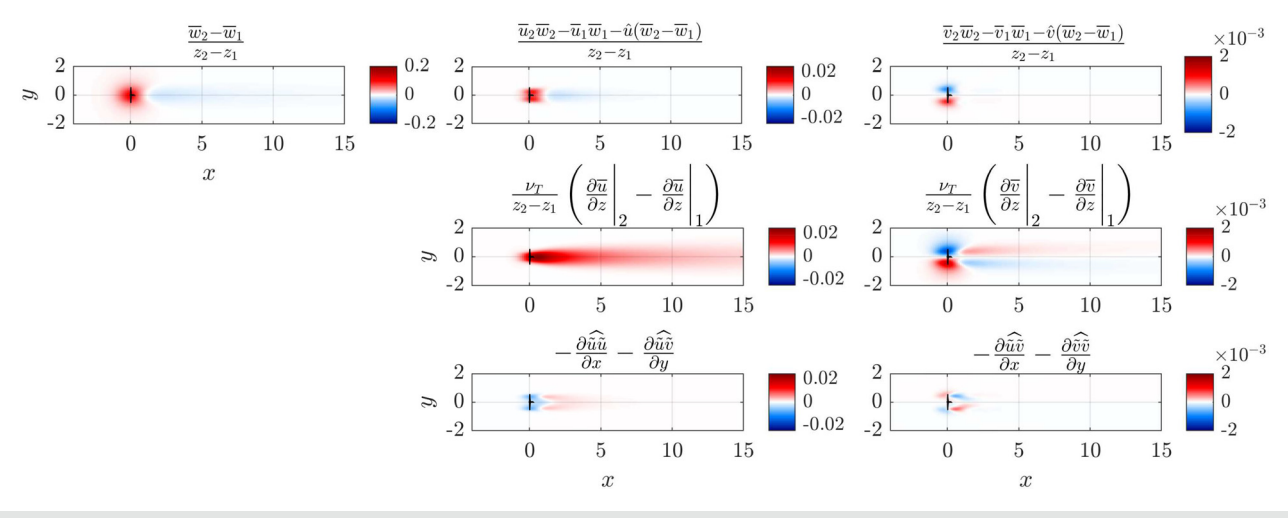


FIG. 14. 3D corrections for the single turbine case [symbols as in Eq. (5)].

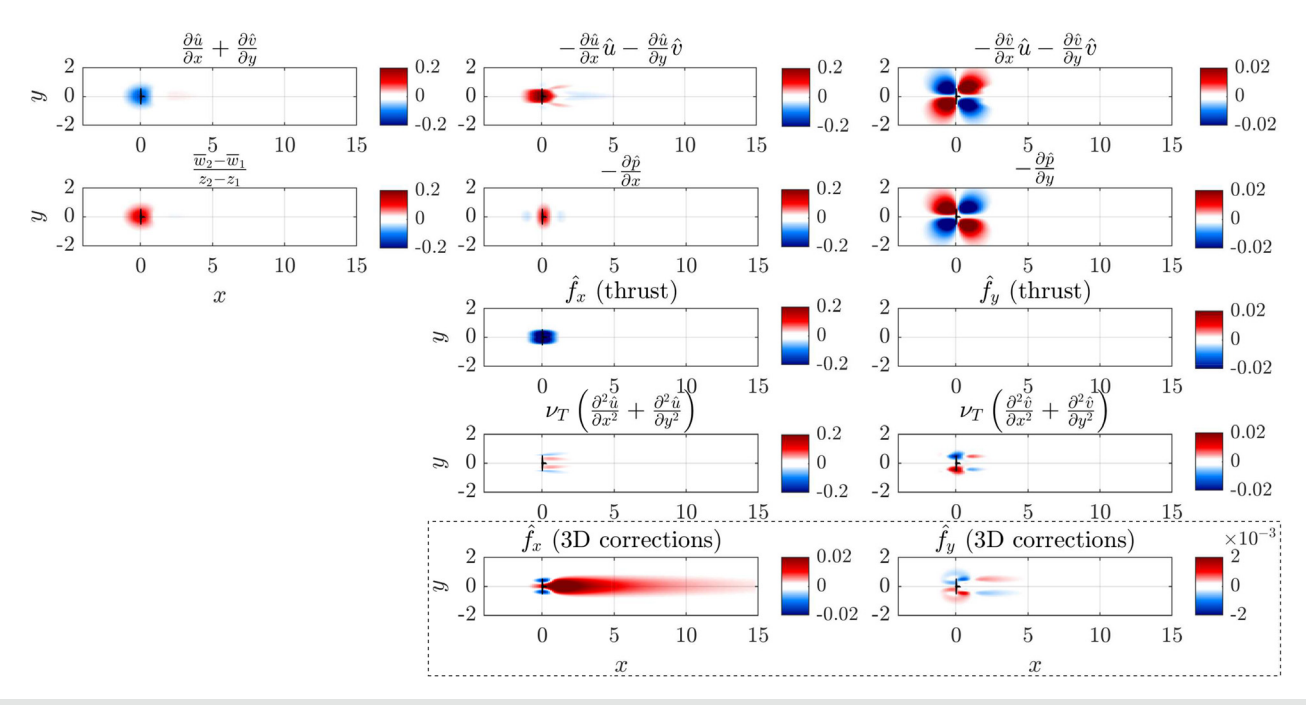


FIG. 15. Breakdown of the individual terms of the P2D RANS equations for the single turbine verification case. The 3D corrections are included in the dashed box, and their colormap limits have been narrowed for better clarity.

 the wind farm efficiency, which is analogous to the previous parameter, yet for the entire turbine array: 125

$$\eta = \frac{\sum_{i=1}^{N_t} P_i(t_j)}{\sum_{i=1}^{N_t} P_{\infty,i}(t_j)},$$
(18)

with $N_t = 25$ turbines for this study;

• the annual (or cumulative) energy loss, which is more relevant from a financial standpoint since it considers the occurrence of

each flow scenario within the local climatology, which can be recast as:

$$\Delta E = \frac{1}{N} \sum_{i=1}^{N} \sum_{i=1}^{N_t} (P_{\infty,i}(t_j) - P_i(t_j)) \cdot 8760, \tag{19}$$

where *N* is the number of available quality controlled data for the flow conditions under consideration and the unit is kWh/y.

The unwaked power for each turbine, $P_{\infty,i}(t_j)$, is defined as the ideal power capture in the absence of wake interactions, and it is estimated through a method similar to that proposed by Farrel *et al.*¹²⁶ to map a heterogeneous wind velocity field over a farm from pointwise

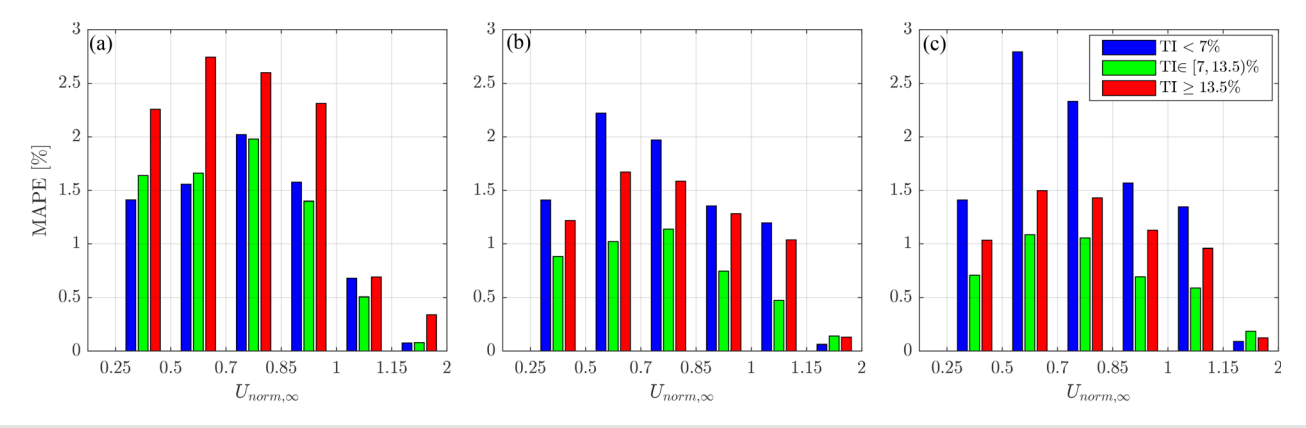


FIG. 16. Mean absolute percentage error of \widehat{u} for between the axisymmetric RANS and the P2D-RANS using different superposition methods for the 3D corrections: (a) linear sum; (b) root-squared signed sum; and (c) maximum absolute value.

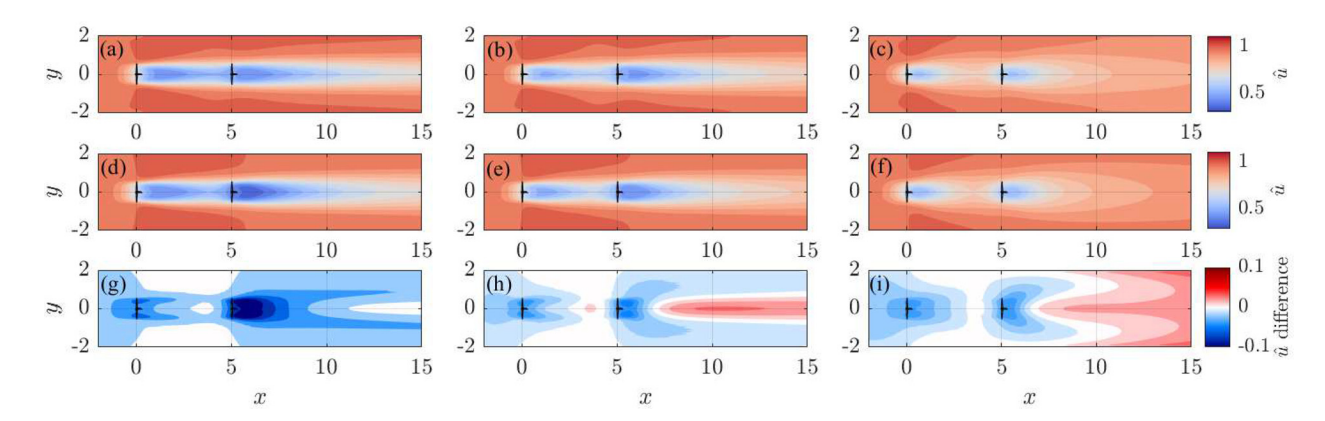


FIG. 17. Streamwise velocity simulated for two in-tandem wind turbines with a streamwise spacing of 5D, $U_{\text{norm},\infty} = 0.775$, and different turbulence intensity levels. By row: (a)–(c) axisymmetric RANS; (d)–(f) P2D-RANS using the root-squared superposition method; (g)–(i) difference (P2D-axisymmetric RANS). By columns: (a), (d), and (g) $TI_{\infty} < 7\%$; (b), (e), and (h) $TI_{\infty} \in (7, 13.5]\%$; (c), (f), and (i) $TI_{\infty} \ge 13.5\%$.

sparse measurements. In this case, the same technique is applied to the power, using the power of unwaked turbines as input. Namely, the power from unwaked turbines [see Fig. 5(a)] is interpolated (extrapolated) at the location of waked turbines through a linear (nearestneighbor) interpolation approach after a Delaunay triangulation. This ensures that the gross power takes into account possible heterogeneity in the wind field over the farm, whose relevance was already confirmed through the power curve analysis (Sec. IV).

It is noteworthy that the occurrence of overpower conditions, i.e., $P_i > P_{\infty,i}$, for a wind farm in flat terrain can be either due to speedups caused by the induction pressure field of neighboring turbines or to an incorrect estimation of $P_{\infty,i}$, which might be associated with low availability of unwaked turbines for a certain wind direction. To exclude this last type of outlier yet retain cases with speedups, cases with overpower higher than 10% are discarded only if the P2D-RANS model indicates that no pressure-induced speedup occurs at that turbine. In other words, the data point is rejected if SCADA data indicate $P_i/P_{\infty,i} > 1.1$ and the P2D-RANS shows $P_i/P_{\infty,i} \leq 1$ (1.3% rejection rate).

Similarly to power, the undisturbed hub-height wind speed, $U_{\text{norm},\infty}$, turbulence intensity, TI_{∞} , and wind direction, θ_w , are estimated as averages of the respective quantities recorded by all the nacelle anemometers (U_{norm} and TI_{∞}) and yaw encoders (θ_w) over the set of unwaked turbines at a specific time, t_j . Cases exhibiting error on the mean over the unwaked turbines at time t_j based on the Student's t distribution¹²⁷ higher than 0.25 for $U_{\text{norm},\infty}$ (0.5% of the overall datasets), 25% of the average value for TI_{∞} (16%), and 5° for θ_w (1.9%) consequent to high flow variability within the park are discarded. Furthermore, periods when more than two turbines are either curtailed (based on the criteria described in Sec. IV) or likely affected by wakes from neighboring turbine arrays that are not modeled are entirely excluded (35%). This slightly relaxed criterion for the rejection of off-design farm operation is beneficial in terms of data availability and has minimal impact on the final statistics.

To showcase the capabilities of the P2D-RANS and highlight the challenges connected with the predictions of power production for individual onshore wind turbines, the simulations of a full day of turbine operation are first analyzed. The simulations are carried out for

operations on August 26, 2016, and use the previously defined undisturbed hub-height wind speed, direction, and turbulence intensity as input with a 10-min resolution. The selected day exhibits the typical stability-driven diurnal cycle of the wind resource,⁷ as shown in Fig. 18. Specifically, the SCADA-recorded and P2D-RANS simulated power capture indicate a generally good agreement, except around 06:00 and 21:00 when the power is overestimated with the P2D-RANS, which is probably a consequence of the inherently complex transition in the atmospheric stability regime. Further insight is gained by selecting four illustrative cases indicated with vertical dashed lines in Fig. 18. For these cases, experimental and numerical wind speed and power capture are reported in Figs. 19 and 20, respectively.

Case 1 represents a typical wind farm operation in region III of the power curve under stable atmospheric conditions and southerly wind direction. Relatively long wakes are observed with a weak velocity deficit [Figs. 19(a) and 19(e)] leading to significant and localized power losses [Figs. 20(a) and 20(e)]. The main challenges in modeling this type of wind farm operation arise from the uncertainty in the quantification of the local wind direction throughout the farm, which is a major source of error in the case of persistent wakes with limited lateral expansion.

Case 2 shows the occurrence of strong wake interactions with relatively small streamwise spacing ($\sim 3D$) associated with moderate westerly winds for operations in region II of the power curve. The proximity of the waked rotors to the complex near-wake turbulent flow of multiple upstream turbines is arguably the most challenging (yet unlikely for a well-designed farm layout) case to simulate. Nevertheless, the P2D-RANS can reproduce satisfactorily the pattern of power losses across the farm [Fig. 20(f)], albeit an evident overestimation in power capture is observed for specific turbines, which may be attributed to the detrimental effect on power capture of partial and/or intermittent wake interaction not reproduced by the steady RANS model.

Case 3 corresponds to highly convective daytime conditions, as portrayed by the utterly complex instantaneous flow field probed by the LiDAR [Fig. 19(c)]. Thanks to the optimally calibrated ν_T , the P2D-RANS model is capable of reproducing the enhanced turbulent mixing of the wakes, which results in moderate yet widespread power

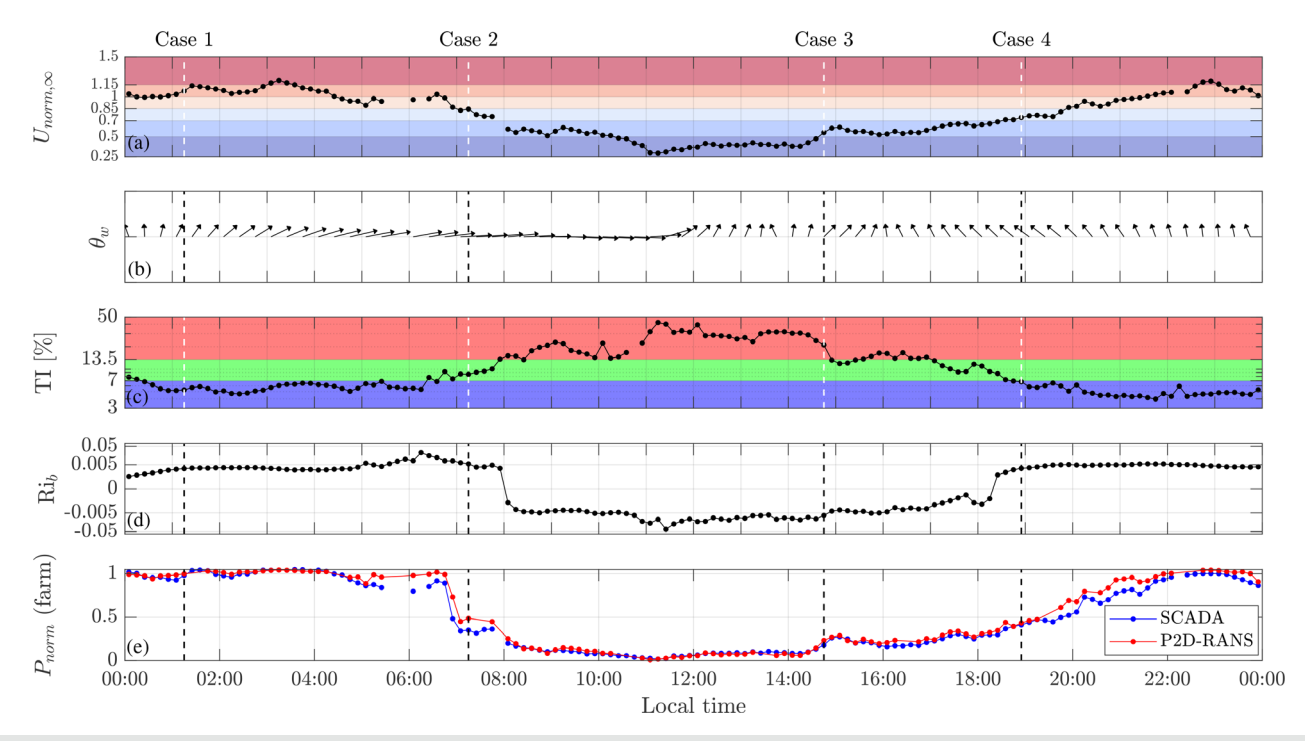


FIG. 18. Inflow characterization for August 26th, 2016: (a) hub-height normalized wind speed; (b) wind direction; (c) turbulence intensity; (d) Bulk Richardson number; and (e) total normalized farm power capture. The background colors in (a) and (c) facilitate the identification of the $U_{\text{norm},\infty}$ and TI_{∞} clusters used in this work.

losses [Fig. 20(g)], in agreement with the respective SCADA data [Fig. 20(c)]. The latter plots also show the occurrence of significant spanwise wind gradient at the southern-most array facing the incoming wind field, which is a quite common phenomenon at this site that justified the formulation of the turbine-specific unwaked power, $P_{\infty,i}$, adopted in Eqs. (17)–(19).

Finally, case 4 represents an interesting south-east wind event, which results in \sim 80% power loss at turbine 07, which is accurately simulated by the P2D-RANS [Figs. 20(d) and 20(h)].

This qualitative analysis is meant to remark the considerable complexity of a real wind farm flow and the challenges inherent to the simulation of the 10-min-averaged power at the single turbine level, at

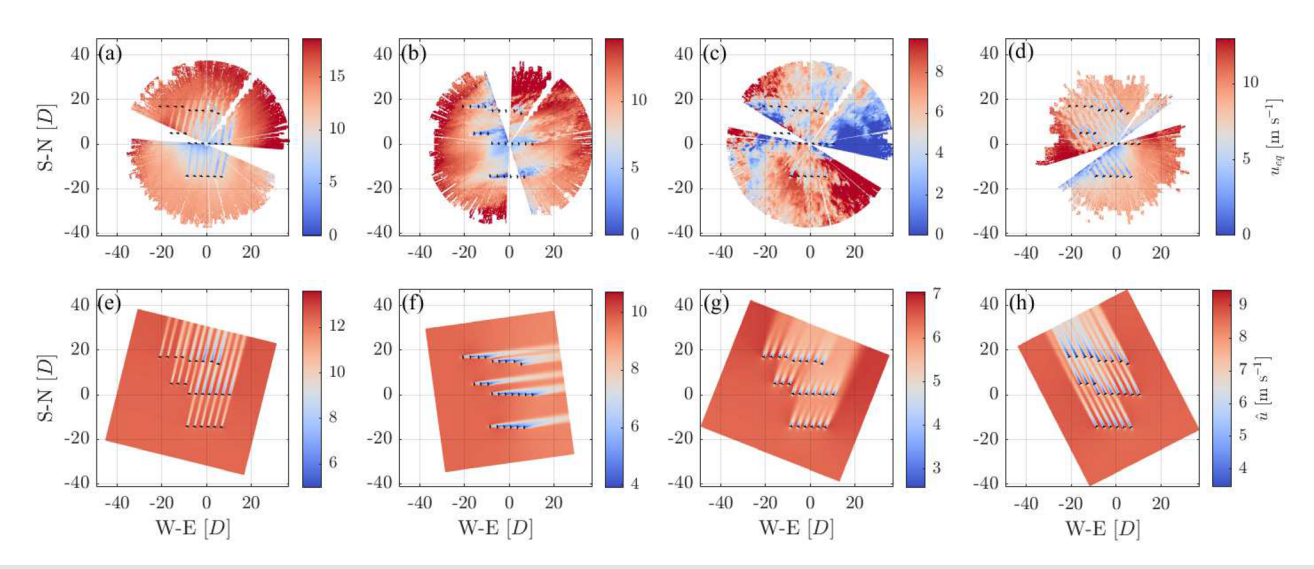


FIG. 19. Horizontal equivalent LiDAR (top row) and depth-averaged P2D-RANS (bottom rows) streamwise velocity for selected 10-min periods on August 26th, 2016: (a) and (e) case 1, 1:10–1:20, $U_{\text{norm},\infty}=1.07$, $\theta_{\text{W}}=194^{\circ}$, $\text{Tl}_{\infty}=5.3\%$; (b) and (f) case 2, 7:10–7:20, $U_{\text{norm},\infty}=0.85$, $\theta_{\text{W}}=262^{\circ}$, $\text{Tl}_{\infty}=8.5\%$; (c) and (g) case 3, 14:40–14:50, $U_{\text{norm},\infty}=0.55$, $\theta_{\text{W}}=202^{\circ}$, $\text{Tl}_{\infty}=21.2\%$; (d) and (h) case 4, 18:50–19:00, $U_{\text{norm},\infty}=0.74$, $\theta_{\text{W}}=156^{\circ}$, $\text{Tl}_{\infty}=6.8\%$;.

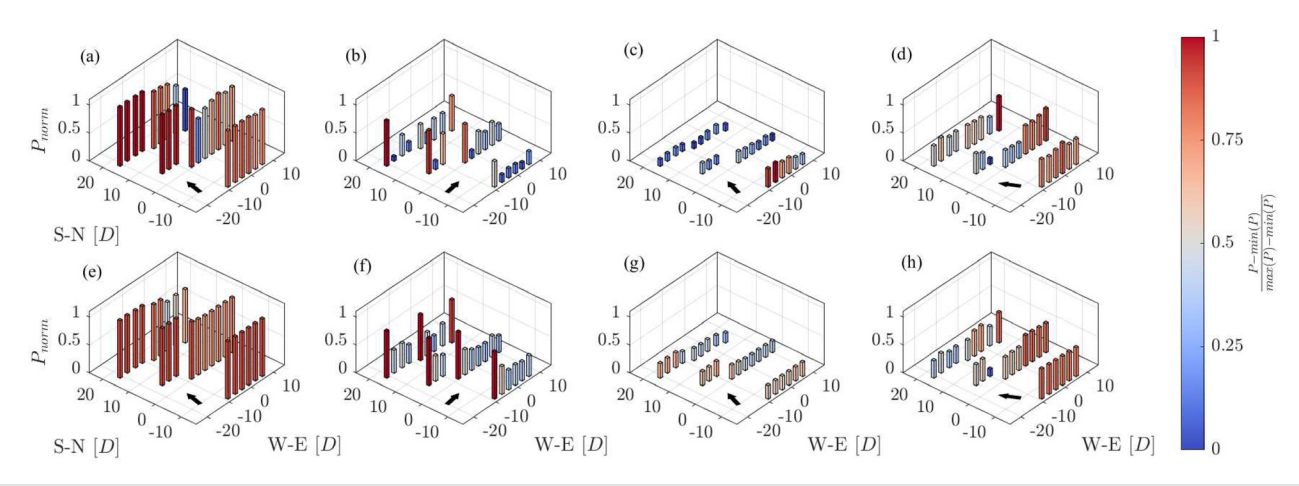


FIG. 20. As in Fig. 19, but for SCADA (top row) and P2D-RANS simulated (bottom row) power capture.

the same time to stress the ability of the P2D-RANS model to reproduce the physical behavior of individual turbines experiencing a real-world turbulent flow, yet keeping the required computational costs and resources very limited.

More systematic quantification of the uncertainty of the P2D-RANS model is carried out through a statistical analysis encompassing all the available SCADA data. To this aim, a lookup table of simulated single-turbine power is built for a wide range of inflow conditions covering the overall climatology of the site. The input inflow matrix is the combination of several $U_{\text{norm},\infty}$ values between 0.2 and 2 (15 cases), TI_{∞} between 4% and 50% (12 cases), and wind directions from 0° to 360° with a resolution of 5°, resulting in 12 960 simulations and a 98.5% coverage of the climatic conditions of the wind farm. A further refinement of the input matrix did not produce any significant differences in the results. The simulated power at the generic time t_j is obtained by interrogating independently for the ith turbine the power lookup table, $P_i(U_{\text{norm},\infty}, TI_{\infty}, \theta_w)$, through a tri-linear interpolation with the experimental values of $U_{\text{norm},\infty}(t_j)$, $TI_{\infty}(t_j)$, and $\theta_w(t_j)$ as inputs.

The characterization of the accuracy of the P2D-RANS in simulating the time-resolved 10-min-averaged power is carried out through a linear regression of the power, as reported in Fig. 21. There is an outstanding agreement for the overall power of the entire farm [Fig. 21(a)] with a negligible bias and $R^2 = 0.998$, which drops when considering the regression between the power of individual turbines [Fig. 21(b), $R^2 = 0.956$]. This feature indicates that a noticeable error cancelation occurs at the farm level, thus making the actual accuracy in power predictions for single turbine power a better indicator to assess the validity of the proposed flow model. For a better understanding of the error source, Figs. 21(c) and 21(d) report the linear regression of single-turbine power for unwaked and waked wind turbines, respectively. It is noteworthy that, although the prediction of the power of waked turbines exhibits larger discrepancies compared to that of unwaked turbines ($R^2 = 0.945$ vs $R^2 = 0.974$), the latter still is encumbered with a non-negligible scattering. This mismatch between the predicted and measured power for unwaked turbines is due to spatial wind gradients, unsteady conditions within the 10-min periods,

power curve uncertainty, and undetected wakes, which represent a baseline error that is inevitably present regardless of the accuracy of the used wind farm model. The linear regression of power capture under waked conditions shows an almost unitary slope and nearly zero intercept, which indicates a negligible contribution of systematic biases in the prediction of the wake interactions to the overall uncertainty.

To provide a more focused statistical analysis of power and energy losses due solely to wake interactions, further validation is performed also including results obtained with the Jensen, 26 Multizone, 43 and Gaussian 33,129 wake models implemented in the FLORIS package. 130 All these models use the nominal power curve (see Fig. 6) and the optimally calibrated c_t reported in Sec. IV, while other wake parameters have default FLORIS settings (specific documentation and references are available at Ref. 130).

First, the ability of the P2D-RANS model to predict the directional wake losses is tested by calculating the bin-average of the percentage power losses for each turbine [Eq. (17)] in 5°-wide sectors, as shown in Fig. 22. Statistics for bins having an error on the mean larger than 25% with 95% confidence are excluded. The model can reproduce the directional pattern of power losses of each turbine satisfactorily with a NMAE = 30.5% with respect to the SCADA data. In Fig. 22, the zoomed-in frame shows how the model can accurately reproduce the wake losses resulting from both near (between turbine 07 and 08, with spacing 4.7D) and far (South direction for turbine 08, with spacing $\sim 15D$) wake interactions, thus confirming the validity of the wake model for a wide range of streamwise distances, even exceeding the domain of LiDAR data used for the calibration.

The zoomed region also indicates that the P2D-RANS provides accurate quantification of the physically consistent overpower occurring at turbine 08 for wind directions at the edge of a heavily waked eastern sector (overpower is visualized as a negative power loss, i.e., the part of the polar plot that lies inside the gray circle corresponding to zero losses). For these cases, the P2D over-performs other engineering wake models, which lack modeling of the pressure field, as the Gaussian wake model (black line in the same plot), and, thus, any

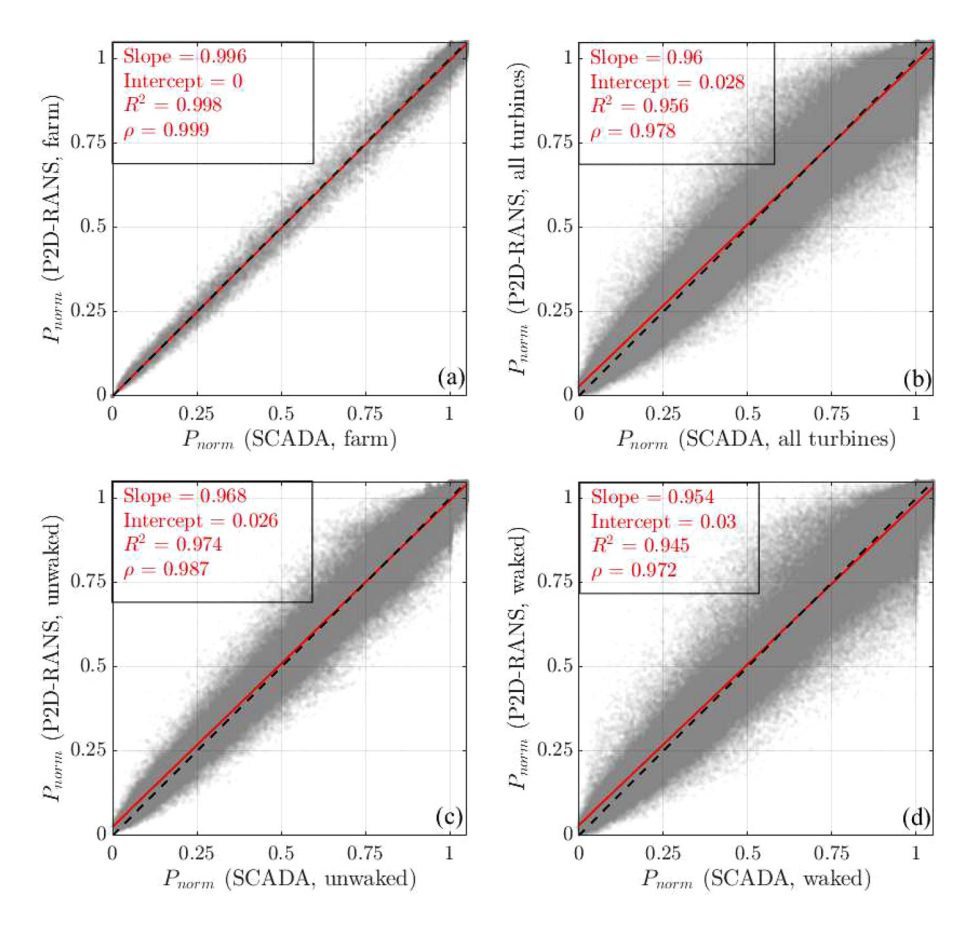


FIG. 21. Linear regression of SCADA vs P2D-RANS 10-min-averaged power: (a) normalized wind farm power; (b) normalized turbine power; (c) normalized power of unwaked turbines; and (d) normalized power of waked turbines.

effect on the incoming wind field induced by the thrust force of a turbine rotor.

The analysis of the wind farm performance as a function of the incoming flow is further refined by bin-averaging the wind farm efficiency, η , for all the wind directions and separately for each $U_{\text{norm},\infty}$

and TI_{∞} cluster (Fig. 23). The resulting directional and clustered wind farm efficiency exhibits, as expected, significant variability with lower values occurring for low $U_{\mathrm{norm},\infty}$ (i.e., high c_t), low TI_{∞} (i.e., slower wake recovery), and winds aligned with the turbine arrays (i.e., W-E direction). This analysis corroborates the high accuracy of the model

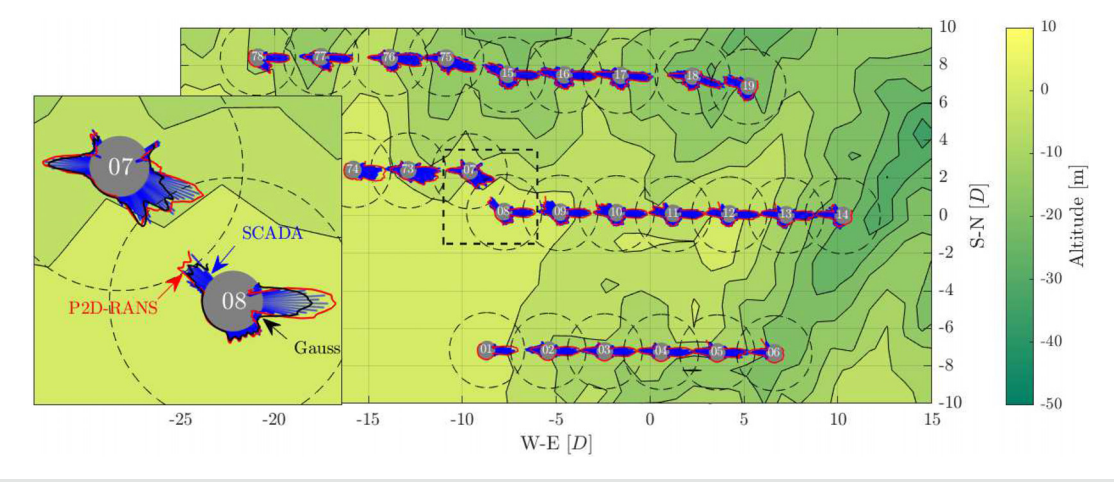


FIG. 22. Polar chart of the directional percentage power losses. The blue bars represent the SCADA data, while the red lines are the P2D-RANS results and the black (zoomed region only) the Gauss model of FLORIS. The gray dots represent the turbines, with the radius corresponding also the $\Delta P_i = 0\%$ losses. The dashed circles indicate $\Delta P_i = 100\%$.

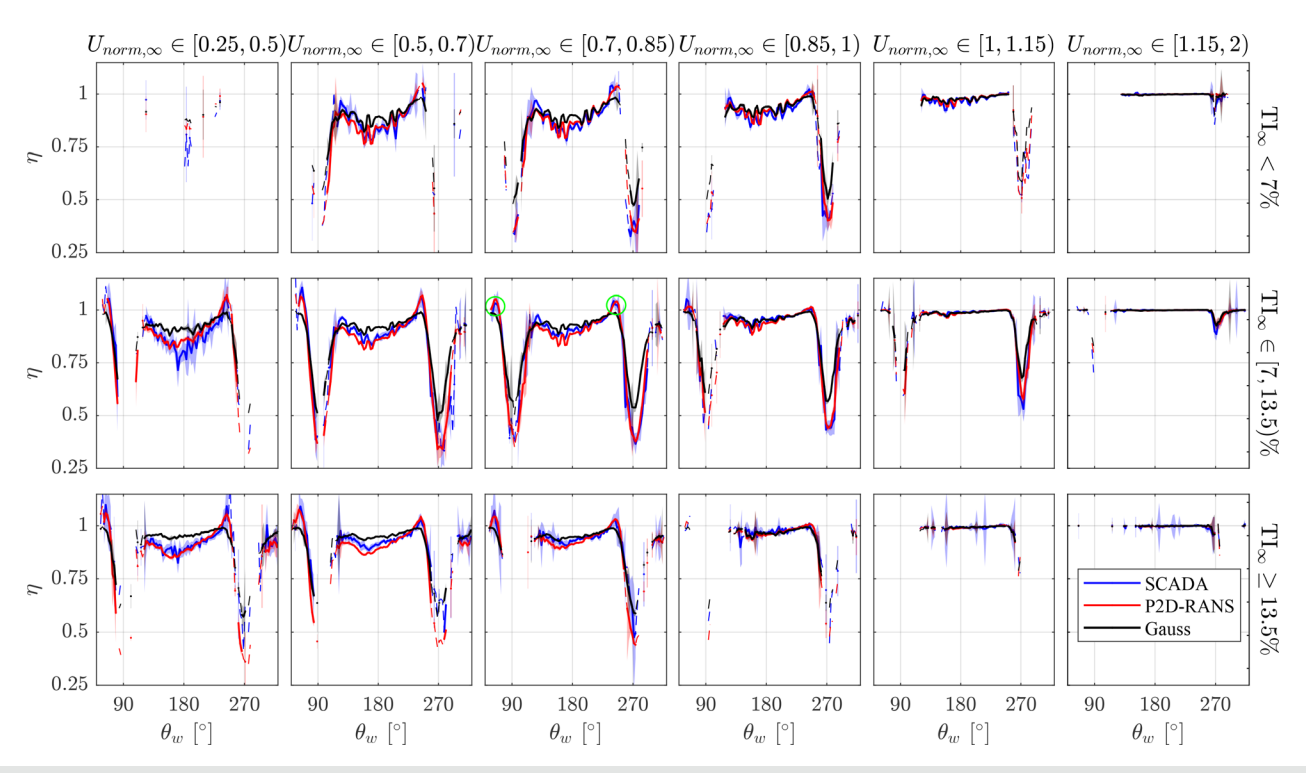


FIG. 23. Directional and clustered wind farm efficiency for all the $U_{\text{norm},\infty}$ and Tl_{∞} clusters defined in Sec. IV). The shaded area represents the error on the mean with 95% confidence level. Dashed lines refer to points rejected due to an error on the mean that exceeds 0.25.

in reproducing the wind farm flow at the turbine level. The Gauss model shows comparatively a poorer agreement with the experimental wind farm efficiency, especially for heavily waked sectors ($\theta_w \sim 90^\circ$ and $\theta_w \sim 270^\circ$), a general underestimation of losses for southerly winds, and a complete lack of wind farm overpower (i.e., $\eta > 1$), which on the contrary is observed for the SCADA and the P2D-RANS for narrow wind sectors around $\theta_w = 65^\circ$ and $\theta_w = 245^\circ$.

In this regard, two occurrences of wind farm efficiency greater than one, which are circled in green in Fig. 23, are further investigated by extracting the individual turbine power gain (i.e., $-\Delta P_i$, which is more suitable to investigate speed-up conditions). Figure 24 displays $-\Delta P_i$ and the non-dimensional wind speed anomaly, $\hat{u}-1$, obtained from the P2D-RANS simulation corresponding to the bin centroids. The visualizations of the wind speed reveal the presence of channeling effects leading to power increases up to $\sim 10\%$, which are also observed in the SCADA data. This is further evidence of the importance of the rotor-induced pressure field on the performance of utility-scale wind turbines.

The influence of the incoming flow on the wind farm performance is further characterized by disregarding power capture variability with the wind direction and calculating clustered wind farm efficiency and annual energy losses associated with the different $U_{\text{norm},\infty}$ and TI_{∞} bins (Fig. 25). The omnidirectional wind farm efficiency exhibits a neat variability for the different TI_{∞} clusters, with higher efficiency achieved for convective conditions, and the expected trend as a function of $U_{\text{norm},\infty}$, as higher losses are observed in region II of the power curve. From the modeling standpoint, the P2D-RANS shows a general slight underestimation of wake losses in stable

atmospheric conditions and overestimation for neutral and convective clusters. Nevertheless, the P2D-RANS achieves better agreement in clustered wind farm efficiency [Fig. 25(a)] and annual energy losses [Fig. 25(e)] than the other wake models considered for this study.

The Jensen model [Figs. 25(b) and 25(f)] generally overestimates the wake losses and does not capture the change in wind farm efficiency due to atmospheric stability. The difference in wind farm efficiency among different TI_{\infty} values is solely due to intra-cluster variability of wind direction, being the analytical wake-field insensitive to the turbulence intensity due to the constant wake expansion coefficient $k_e = 0.05$. The Multizone model [Figs. 25(c) and 25(g)] also fails to fully capture the effect of the atmospheric stability, since it still uses a fixed wake expansion coefficient $k_e = 0.05$. The overestimation of wake losses is however assuaged thanks to the improved formulation of the velocity field, compared to Jensen. The Gaussian model with the TI-dependent wake expansion 131 $k_e = 0.004 + 0.38$ TI $_{\infty}$ shows a significant improvement, although it generally underestimates the wake losses in region II of the power curve. The performance of the Gaussian model is remarkable, considering the extremely low computational time (0.1 s per simulation) and the lack of a site-specific calibration of the wake expansion coefficient.

The NMAE for all the performance indicators presented in this section are summarized in Fig. 26 and for all the models. Although the P2D-RANS shows the smallest error for all the statistics, there are important distinctions that it is worth pointing out. Table V provides the percentage improvement attained by the P2D-RANS compared to the other wake models to assist the interpretation of the results. The P2D-RANS achieves a significant

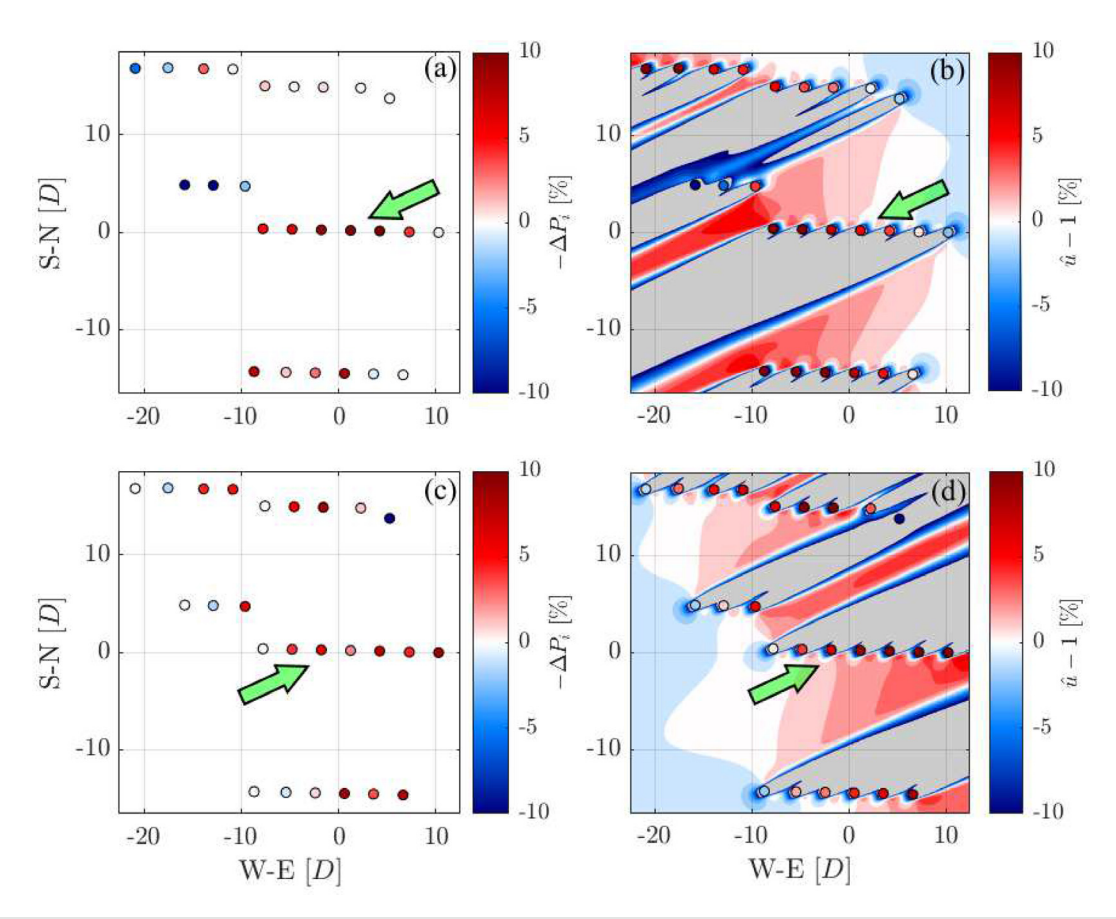


FIG. 24. Power gain for selected wind direction bins within the cluster $U_{\mathsf{norm},\infty} \in [0.7, 0.85)$, $\mathsf{TI}_\infty \in [7, 13.5)\%$: (a) SCADA power gain for $\theta_\mathsf{w} \in [62.5, 67.5)^\circ$; (b) P2D-RANS power gain for $\theta_\mathsf{w} \in (62.5, 67.5)^\circ$; (c) SCADA power gain for $\theta_\mathsf{w} \in [242.5, 247.5)^\circ$; and (d) P2D-RANS power gain for $\theta_\mathsf{w} \in (242.5, 247.5)^\circ$. The velocity fields in (b) and (d) corresponds to the P2D-RANS solution for the bin centroid.

reduction of error for the farm and single-turbine power (especially waked turbines) compared to Jensen and Multizone, while the improvement compared to the more accurate TI-dependent Gaussian model is more limited (8% for the single turbine power). Better relative performances are observed for the directional single-turbine power losses, with a 22% error reduction achieved by the P2D-RANS compared to the Gaussian model, a consequence of the more accurate description of the wake velocity field and the modeling of the rotor-induced pressure field and the associated speed-up conditions for specific wind directions. A further significant margin of improvement is obtained for the statistics taking into account atmospheric stability through the clustering in TI_{∞} , which is a clear indication that the site-specific calibration of ν_T is beneficial. The NMAE reduction with respect to the Gaussian model is 24% for the directional and clustered wind farm efficiency and 40% for the annual energy losses. This last parameter is particularly relevant for the quantification of the financial losses due to wake interactions at a specific site. Therefore, the significantly enhanced accuracy in the prediction of the energy losses achieved by the P2D-RANS compared to other models is required to justify the investment in such LiDAR-driven CFD approach, which is

computationally and logistically more expensive than the other engineering wake models.

For the sake of completeness, the gross and net capacity factors and the overall wake losses for the full SCADA dataset are reported in Table VI. The P2D-RANS is still the model giving the best prediction; nevertheless its capability in simulating the wake interaction under different atmospheric stability and operative conditions is not clearly identifiable using these global statistical parameters.

VII. CONCLUSIONS

The theoretical fundamentals, numerical scheme, verification, and validation process of the Pseudo 2D-RANS (P2D-RANS) model have been discussed in this manuscript. The P2D-RANS uses a shallow-water approximation of the RANS equations to achieve an efficient solution of a wind farm flow vertically averaged over the rotor heights by inserting into the RANS solver appropriate corrective source terms, which take into account the contribution to the mass and momentum budgets of vertical fluxes and spatial dispersive

The set of depth-averaged and corrected flow equations is solved through an iterative marching scheme, which alternates sweeps in the

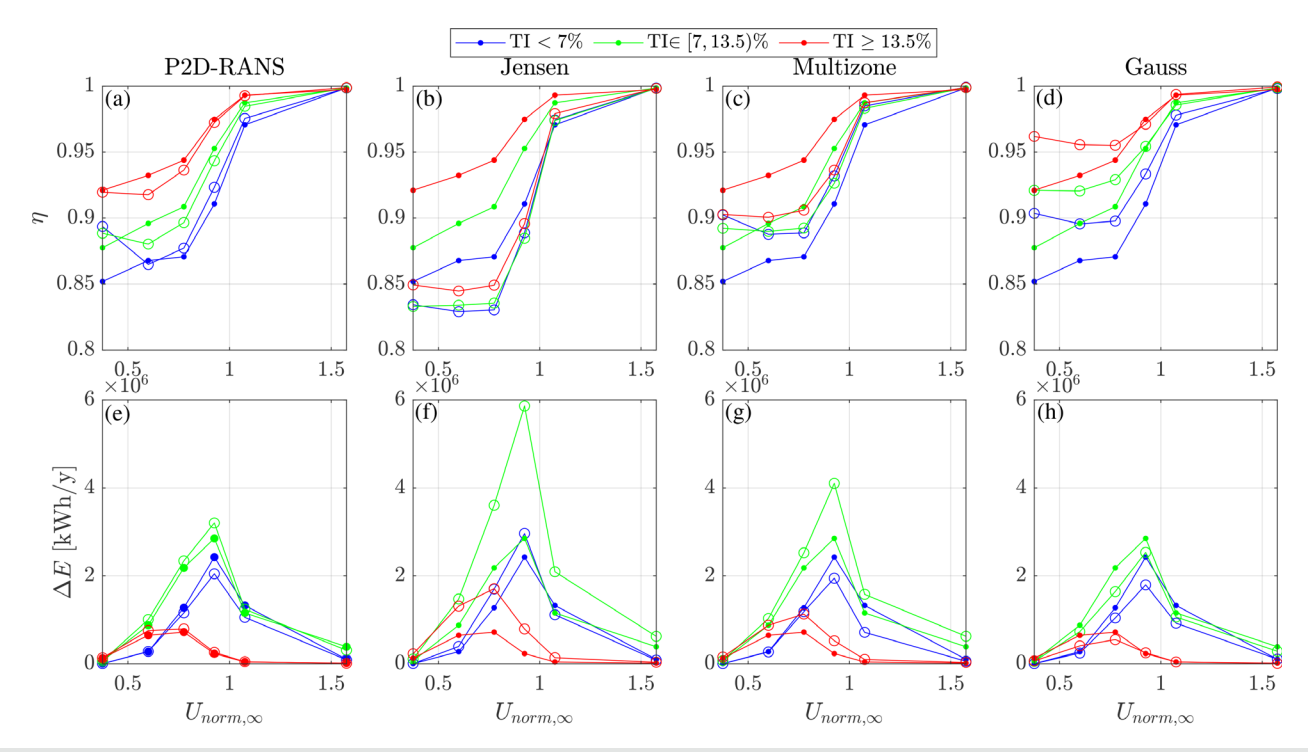


FIG. 25. Clustered wind farm efficiency (a)–(d) and annual energy losses (e)–(h) obtained with the P2D-RANS (a) and (e), Jensen model (b) and (f), Multizone model (c) and (g), and the Gaussian model (d) and (h). The dots indicate the SCADA statistics; the empty circles refer to the models. All points displayed satisfy the requirement of less than 25% of error on the mean with a 95% confidence.

streamwise directions for the solution of the momentum equations and global pressure corrections to ensure a solenoidal velocity field upon the convergence of the algorithm. The detailed derivation of the pressure correction, which may represent a generalizable and convenient numerical tool for the solution of partially parabolized flows with source terms, is also provided.

Clustered and statistically analyzed LiDAR measurements of wakes generated by utility-scale wind turbines have been leveraged to calibrate the turbulence closure and the actuator disk models implemented into the P2D-RANS. The optimally tuned turbulent eddyviscosity exhibits physically reasonable trends as a function of the turbulence intensity of the incoming wind with a striking wake recovery enhancement detected for convective conditions, which might be connected with the occurrence of wake meandering. The thrust-force distribution over the rotor radial direction has been estimated for the various bins of incoming wind speed and turbulence intensity at hub

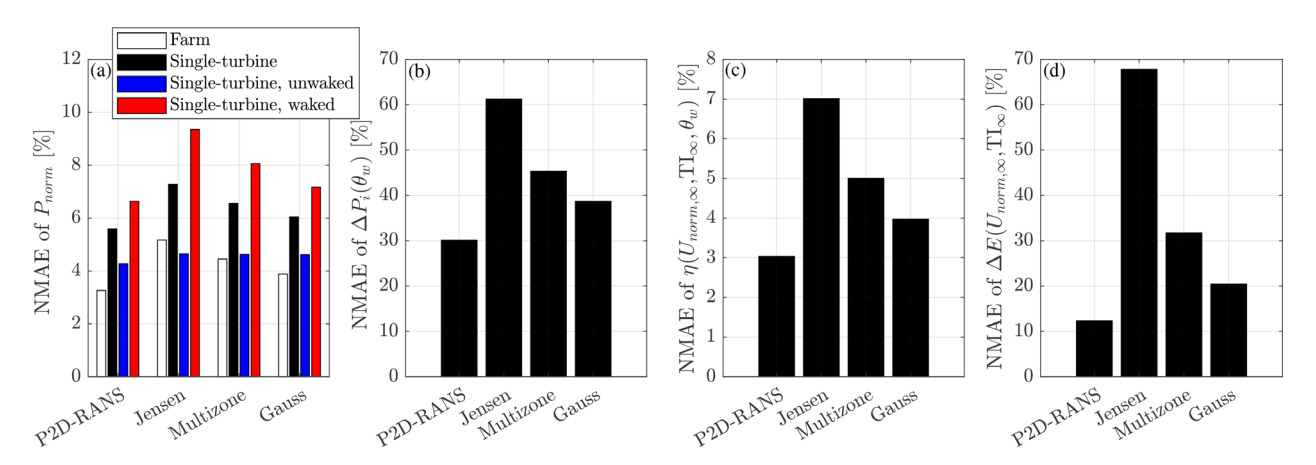


FIG. 26. Normalized mean absolute error (NMAE) for the different performance indicator of the P2D-RANS and FLORIS wake models: (a) power capture; (b) single-turbine directional percentage power losses; (c) directional and clustered wind farm efficiency; and (d) clustered annual energy losses.

TABLE V. Percentage improvement in NMAE of the P2D-RANS model compared to the FLORIS wake models.

	Jensen	Multizone	Gauss
P _{norm} (farm)	37	27	16
P_{norm} (single-turbine)	23	15	8
P _{norm} (single-turbine, unwaked)	8	8	7
P_{norm} (single-turbine, waked)	29	18	8
$\Delta P_i(\theta_w)$	51	33	22
$\eta(U_{\mathrm{norm},\infty},\mathrm{TI}_{\infty}, heta_w)$	57	39	24
$\Delta E(U_{ m norm,\infty}, { m TI}_{\infty})$	82	61	40

height. This data-driven approach has enabled the detection of a general reduction of the thrust force when turbine operations transition from region II to region III of the power curve.

The correctness of the conceptual and computational framework of the P2D-RANS and its numerical implementation has been verified vs the solution of an elliptic axisymmetric RANS solver for single and in-tandem wind turbines. The validation process of the P2D-RANS has been broken down into three phases. First, effects of the daily cycle of the atmospheric stability on operations of an onshore farm have been simulated with a 10-min resolution and then assessed against the SCADA data at the single-turbine level. Subsequently, the 10-minaveraged power has been simulated for the whole set of available SCADA data to perform statistically meaningful error analysis. The power of single turbines shows an $R^2 = 0.956$, a normalized mean absolute error of 5.6%, and negligible bias, which represents an 8% error reduction compared to the Gaussian wake model. Finally, wake losses have been quantified through different indicators and extensively analyzed as a function of the inflow conditions. The P2D-RANS reproduces satisfactorily the single-turbine directional wake losses, including the effect of a local increase in the freestream wind speed, referred to as flow speed-up conditions, which are induced by the rotor pressure field for specific wind directions. Such speed-up conditions have also repercussions on the wind farm efficiency, which is predicted with a normalized mean absolute error of 3% and 24% smaller than for the Gaussian model.

The P2D-RANS reproduces convincingly the annual energy wake losses (12% error) for different stability and operative conditions, which indicates the financial relevance of LiDAR-driven CFD modeling in the context of the optimal design of wind farms. It is also proven the necessity for correct modeling of the variability of wind farm efficiency with atmospheric stability.

The current implementation of the P2D-RANS can solve the steady flow over a wind farm with 25 turbines and extending 30D by

TABLE VI. Gross capacity factor, net capacity factor, and wake loss factor estimated with the various wind farm models.

	SCADA	P2D-RANS	Jensen	Multizone	Gauss
Gross capacity factor	0.801	0.800	0.799	0.799	0.800
Net capacity factor	0.77	0.768	0.746	0.763	0.774
Wake losses (%)	3.87	4.00	6.63	4.51	3.25

30D in an averaged time of ~ 80 s on a commercial laptop equipped with a single i5 1.70 GHz core, which can enable performing real-time wind farm monitoring and control. The required computational time has been observed to be roughly half when operating an Intel Xeon Platinum 8160 48-core 2.1 GHz cluster, which implies that the full characterization of the performances of a mid-sized farm can be completed in ~ 170 CPU-hours.

ACKNOWLEDGMENTS

This material is based upon work supported by the National Science Foundation (Grant No. IIP-1362022; Collaborative Research - I/UCRC for Wind Energy, Science, Technology, and Research) and from the WindSTAR I/UCRC Members of Aquanis, Inc., EDP Renewables, Bachmann Electronic Corp., GE Energy, Huntsman, Hexion, Leeward Asset Management, LLC, Pattern Energy, EPRI, LMWind, Texas Wind Tower, and TPI Composites. This research has been funded by the National Science Foundation CBET Fluid Dynamics (Grant No. 1705837).

AUTHOR DECLARATIONS

Conflict of Interest

The authors have no conflicts to disclose.

DATA AVAILABILITY

Data sharing is not applicable to this article as no new data were created or analyzed in this study.

APPENDIX A: ESTIMATION OF 3D CORRECTION FOR AN AXISYMMETRIC FLOW

The 3D and dispersive terms in Eq. (5) are estimated assuming an axisymmetric, non-swirling flow. By setting the boundary of the domain to $z_1 = -D/2$ and $z_2 = D/2$, the unknown 3D terms can be conveniently recast as follows:

$$\frac{\left|\frac{\bar{w}_{2} - \bar{w}_{1}}{z_{2} - z_{1}}\right|}{z_{2} - z_{1}} = \frac{w_{D/2}}{D/2},
\frac{\bar{u}_{2}\bar{w}_{2} - \bar{u}_{1}\bar{w}_{1} - \hat{u}(\bar{w}_{2} - \bar{w}_{1})}{z_{2} - z_{1}} = \frac{(\bar{u}_{D/2} - \hat{u})\bar{w}_{D/2}}{D/2},
\frac{\nu_{T}}{z_{2} - z_{1}} \left(\frac{\partial \bar{u}}{\partial z}\Big|_{2} - \frac{\partial \bar{u}}{\partial z}\Big|_{1}\right) = \frac{\nu_{T}}{D/2} \frac{\partial \bar{u}}{\partial z}\Big|_{D/2},
\frac{\bar{v}_{2}\bar{w}_{2} - \bar{v}_{1}\bar{w}_{1} - \hat{v}(\bar{w}_{2} - \bar{w}_{1})}{z_{2} - z_{1}} = \frac{(\bar{v}_{D/2} - \hat{v})\bar{w}_{D/2}}{D/2},
\frac{\nu_{T}}{z_{2} - z_{1}} \left(\frac{\partial \bar{v}}{\partial z}\Big|_{2} - \frac{\partial \bar{v}}{\partial z}\Big|_{1}\right) = \frac{\nu_{T}}{D/2} \frac{\partial \bar{v}}{\partial z}\Big|_{D/2}.$$
(A1)

The depth-average $\widehat{\cdot}$ is related to the 3D field by the operator defined in Eq. (4).

Under the assumption of axisymmetric flow, the 3D field $\bar{u}(x_i,y_j,z_k)$ can be obtained by sampling the streamwise velocity component expressed in cylindrical coordinates, $\bar{u}_x(x,r)$ at $x=x_i$ and radial location $r_l=\sqrt{y_j^2+z_j^2}$ (see Fig. 27). Formalizing the sampling operation from the radial location r_l to the Cartesian equivalent (y_i,z_k) as a linear interpolation operator, Φ , yields

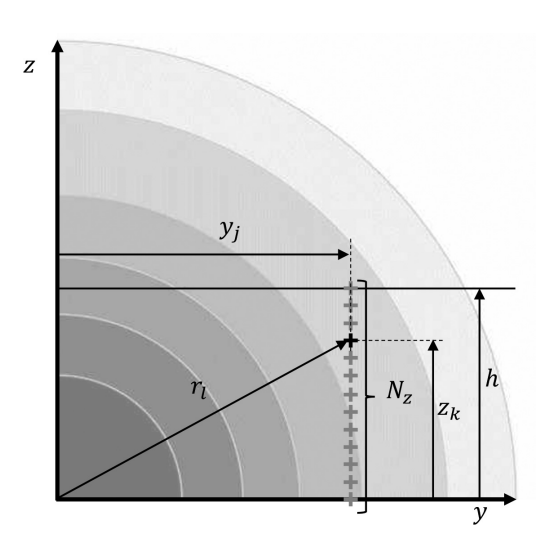


FIG. 27. Sampling of the axisymmetric streamwise velocity for the calculation of the depth average. The iso-levels in the background indicate the magnitude of the axisymmetric velocity field, \bar{u}_x , which is sampled to calculate \tilde{u} .

$$\widehat{u}_{ij} = \frac{1}{N_z} \sum_{k=1}^{N_z} \bar{u}(x_i, y_j, z_k)
= \frac{1}{N_z} \sum_{k=1}^{N_z} \bar{u}_x \left(x_i, \sqrt{y_j^2 + z_k^2} \right)
= \frac{1}{N_z} \sum_{k=1}^{N_z} \sum_{l=1}^{N_r} \Phi_{k,l} \bar{u}_{x,il} \Rightarrow \widehat{u} = M_u(\bar{u}_x).$$
(A2)

Similarly, for the depth-averaged transverse velocity, one can show that:

$$\widehat{\nu}_{ij} = \frac{1}{N_z} \sum_{k=1}^{N_z} \sum_{l=1}^{N_r} \frac{y_j}{r_l} \Phi_{k,l} \bar{u}_{r,il} \Rightarrow \widehat{\nu} = M_{\nu}(\bar{u}_r). \tag{A3}$$

It is noteworthy that the linear operators M_u and M_v of Eqs. (A2) and (A3) are invertible, namely, it always possible to calculate from a depth-averaged velocity (i.e., the P2D-RANS provisional solution) the equivalent axisymmetric velocity field without swirl.

APPENDIX B: DERIVATION OF THE PRESSURE CORRECTION

To derive the pressure correction, the velocity, and pressure fields at the current iteration are separated into two components:

- the provisional field (\$\hat{u}\$, \$\hat{v}\$, and \$\hat{p}\$), in which the velocity components satisfy the momentum equation with the currently estimated pressure \$\hat{p}\$;
- (2) the correction field $(\widehat{u}^c, \widehat{v}^c, \text{and } \widehat{p}^c)$, that is added to the provisional field to satisfy the continuity equation.

By assuming that the correction field is much smaller than the main field, i.e., $\hat{u}^c \ll \hat{u}$, $\hat{v}^c \ll \hat{v}$, $\hat{p}^c \ll \hat{p}$, and considering that the main field satisfies the RANS equations [Eq. (5)], one can recast the correction field equations as

$$\begin{cases}
\widehat{u}\frac{\partial \widehat{u}^{c}}{\partial x} + \widehat{v}\frac{\partial \widehat{u}^{c}}{\partial y} + \widehat{u}^{c}\frac{\partial \widehat{u}}{\partial x} + \widehat{v}^{c}\frac{\partial \widehat{u}}{\partial y} = -\frac{\partial \widehat{p}^{c}}{\partial x} + \nu_{T}\left(\frac{\partial^{2}\widehat{u}^{c}}{\partial x^{2}} + \frac{\partial^{2}\widehat{u}^{c}}{\partial y^{2}}\right) \\
\widehat{u}\frac{\partial \widehat{v}^{c}}{\partial x} + \widehat{v}\frac{\partial \widehat{v}^{c}}{\partial y} + \widehat{u}^{c}\frac{\partial \widehat{v}}{\partial x} + \widehat{v}^{c}\frac{\partial \widehat{v}}{\partial y} = -\frac{\partial \widehat{p}^{c}}{\partial y} + \nu_{T}\left(\frac{\partial^{2}\widehat{v}^{c}}{\partial x^{2}} + \frac{\partial^{2}\widehat{v}^{c}}{\partial y^{2}}\right).
\end{cases}$$
(B1)

Taking the divergence of Eq. (B1) yields

$$\widehat{u}^{c} \frac{\partial (\nabla \cdot \widehat{\mathbf{u}})}{\partial x} + \widehat{v}^{c} \frac{\partial (\nabla \cdot \widehat{\mathbf{u}})}{\partial y} + \widehat{u} \frac{\partial (\nabla \cdot \widehat{\mathbf{u}}^{c})}{\partial x} + \widehat{v} \frac{\partial (\nabla \cdot \widehat{\mathbf{u}}^{c})}{\partial y} \\
= + \gamma (\widehat{u}, \widehat{v}, \widehat{u}^{c}, \widehat{v}^{c}) - \frac{\partial^{2} \widehat{p}^{c}}{\partial x^{2}} - \frac{\partial^{2} \widehat{p}^{c}}{\partial y^{2}} \\
+ \nu_{T} \left(\frac{\partial^{2} (\nabla \cdot \widehat{\mathbf{u}}^{c})}{\partial x^{2}} + \frac{\partial^{2} (\nabla \cdot \widehat{\mathbf{u}}^{c})}{\partial y^{2}} \right), \tag{B2}$$

where

$$\gamma(\widehat{u},\widehat{v},\widehat{u}^c,\widehat{v}^c) = 2\left(\frac{\partial \widehat{u}}{\partial x}\frac{\partial \widehat{u}^c}{\partial x} + \frac{\partial \widehat{v}}{\partial y}\frac{\partial \widehat{v}^c}{\partial y} + \frac{\partial \widehat{v}}{\partial x}\frac{\partial \widehat{u}^c}{\partial y} + \frac{\partial \widehat{v}^c}{\partial x}\frac{\partial \widehat{u}^c}{\partial y}\right). \tag{B3}$$

For the corrected fields to be solenoidal, the following equality must be satisfied

$$\nabla \cdot \widehat{\mathbf{u}}^{c} = -\nabla \cdot \widehat{\mathbf{u}} - \frac{\overline{w}_{2} - \overline{w}_{1}}{z_{2} - z_{1}} = -\nabla.$$
 (B4)

Equation (B4) implies that even though $|\widehat{\mathbf{u}}^{\mathbf{c}}| \ll |\widehat{\mathbf{u}}|$, the divergence of both fields has the same magnitude. This allows neglecting the first two terms of the LHS of Eq. (B2):

$$-\widehat{u}\frac{\partial \nabla}{\partial x} - \widehat{v}\frac{\partial \nabla}{\partial y} + \gamma \sim -\frac{\partial^2 \widehat{p}^c}{\partial x^2} - \frac{\partial^2 \widehat{p}^c}{\partial y^2} - \nu_T \left(\frac{\partial^2 \nabla}{\partial x^2} + \frac{\partial^2 \nabla}{\partial y^2}\right). \quad (B5)$$

The correction velocity components are unknown, so the term γ defined in Eq. (B3) is necessarily dropped, 105,132 which yields the final results reported as Eq. (8). The error associated with this approximation is eventually reduced by applying the correction iteratively. The RHS of the pressure correction [Eq. (9)] contains an advection term and a diffusion term. The former creates a positive (negative) local pressure if a certain material volume of fluid is undergoing compression (expansion), while the latter creates a positive (negative) local pressure if a region of fluid is locally experiencing compression (expansion). The latter induces a pressure maximum (minimum) if the flow is locally experiencing a compression (expansion). Nonetheless, the pressure correction guides the solution toward a divergence-free velocity field. Figure 28 shows graphically the behavior of the pressure correction, \hat{p}^c , in response to a local compression.

APPENDIX C: LOAD FORMULATION

The non-dimensional streamwise momentum sink used to mimic the action of the generic *i*th rotor on the flow in the P2D-RANS is defined as

$$\widehat{f}_{x,i} = cs(x)\widehat{\phi}(y)\widehat{u}^2(x_{0,i}, y), \tag{C1}$$

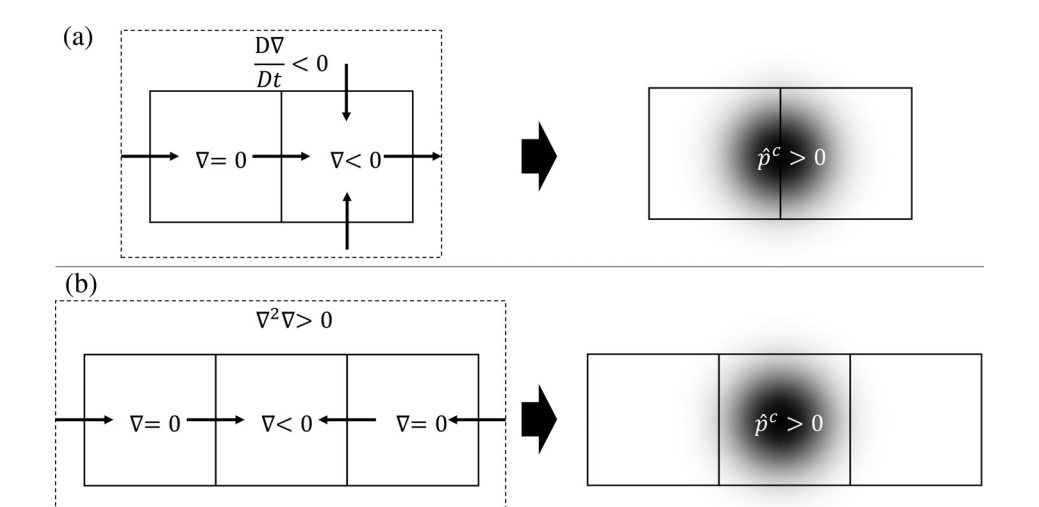


FIG. 28. Graphical representation of the effect of the LHS of Eq. (9) on pressure correction: (a): advection term; (b) diffusion term.

where c is a normalization constant, s(x) is a Gaussian smoothing kernel with standard deviation 0.5D, $\widehat{\phi}(y)$ is a shape function containing the information on the radial distribution of the axial induction, and $x_{0,i}$ is the sampling location 2D upstream of the turbine where the freestream velocity is extracted. Specifically, the freestream velocity is defined as the rotor-averaged \widehat{u} . The introduction of the $\widehat{u}^2(x_{0,i},y)$ modulates the local thrust in the case of non-uniform inflow and enhances numerical stability by preventing reverse flow. The normalization constant is obtained by imposing the total thrust to equate the one dictated by the LiDAR-driven c_t as follows:

$$c \int_{-0.5}^{0.5} \widehat{\phi}(y) \widehat{u}^{2}(x_{0,i}, y) \left[\int_{+\infty}^{-\infty} s(x) dx \right] dy = \frac{\frac{1}{2} \rho c_{t} \pi \frac{D^{2}}{4} U_{\infty,i}^{2}}{\rho U_{\infty}^{2} D^{2}}, \quad (C2)$$

where $U_{\infty,i}$ is the dimensional local incoming wind speed, defined as the average of the streamwise velocity over the rotor span at $x_{0,i}$. Since that s(x) has unit integral, the former equality yields

$$c = \frac{\pi c_t}{8 \int_{0.5}^{0.5} \widehat{\phi}(y) \widehat{u}^2(x_{0,i}, y)} \left(\frac{U_{\infty,i}}{U_{\infty}}\right)^2.$$
 (C3)

In the case of uniform inflow, the former equation reduces to

$$c = \frac{\pi c_t}{8 \int_{-0.5}^{0.5} \widehat{\phi}(y)}.$$
 (C4)

REFERENCES

¹J. Sanz Rodrigo, R. A. Chávez Arroyo, P. Moriarty, M. Churchfield, B. Kosović, P. E. Réthoré, K. S. Hansen, A. Hahmann, J. D. Mirocha, and D. Rife, "Mesoscale to microscale wind farm flow modeling and evaluation," Wiley Interdiscip. Rev. 6, e214 (2017).

²F. Porté-agel, M. Bastankhah, and S. Shamsoddin, "Wind-turbine and windfarm flows: A review," Boundary-Layer Meteorol. 174, 1–59 (2019).

³P. Veers, K. Dykes, E. Lantz, S. Barth, C. Bottasso, O. Carlson, A. Clifton, J. Green, P. Green, H. Holttinen, D. Laird, V. Lehtomäki, J. Lundquist, J. Manwell, M. Marquis, C. Meneveau, P. Moriarty, X. Munduate, M. Muskulus, J. Naughton, L. Pao, J. Paquette, J. Peinke, A. Robertson, J. S. Rodrigo, A. Sempreviva, J. Smith, A. Tuohy, and R. Wiser, "Grand challenges in the science of wind energy," Science 366, aau2027 (2019).

⁴M. Christiansen and C. Hasager, "Using airborne and satellite SAR for wake mapping offshore," Wind Energy 9, 437–455 (2006).

⁵A. Platis, S. Siedersleben, J. Bange, A. Lampert, K. Bärfuss, R. Hankers, B. Cañadillas, R. Foreman, J. Schulz-Stellenfleth, B. Djath, T. Neumann, and S. Emeis, "First *in situ* evidence of wakes in the far field behind offshore wind farms," Sci. Rep. **8**, 2163 (2018).

⁶J. Lundquist, K. DuVivier, D. Kaffine, and J. Tomaszewski, "Costs and consequences of wind turbine wake effects arising from uncoordinated wind energy development," Nat. Energy 4, 26–34 (2019).

7S. El-Asha, L. Zhan, and G. Iungo, "Quantification of power losses due to wind turbine wake interactions through SCADA, meteorological and wind LiDAR data," Wind Energy 20, 1823–1839 (2017).

⁸D. Conti, N. Dimitrov, and A. Peña, "Aeroelastic load validation in wake conditions using nacelle-mounted lidar measurements," Wind Energy Sci. 5, 1129–1154 (2020).

⁹B. H. Bailey, "The financial implications of resource assessment," Technical Report (TruePower, 2014), https://www.sewind.org/presentations/2014/2014-07-24_SECWC_Workshop_Presentation-Bruce_Bailey.pdf.

¹⁰R. Barthelmie, S. Pryor, S. Frandsen, K. Hansen, J. Schepers, K. Rados, W. Schelz, A. Neubert, L. Jensen, and S. Neckelmann, "Quantifying the impact of wind turbine wakes on power output at offshore wind farms," J. Atmos. Ocean. Technol. 27, 1302–1317 (2010).

¹¹A. Sebastiani, F. Castellani, G. Crasto, and A. Segalini, "Data analysis and simulation of the Lillgrund wind farm," Wind Energy 24, 634–648 (2020).

¹²M. Magnusson and A. Smedman, "Influence of atmospheric stability on wind turbine wakes," Wind Eng. 18, 139–152 (1994).

¹³G. V. Iungo and F. Porté-Agel, "Volumetric lidar scanning of wind turbine wakes under convective and neutral atmospheric stability regimes," J. Atmos. Oceanic Technol. 31, 2035–2048 (2014).

¹⁴F. Carbajo Fuertes, C. D. Markfort, and F. Porté-Agel, "Wind turbine wake characterization with nacelle-mounted wind lidars for analytical wake model validation," Remote Sens. 10, 668 (2018).

¹⁵L. Zhan, S. Letizia, and G. Valerio Iungo, "Lidar measurements for an onshore wind farm: Wake variability for different incoming wind speeds and atmospheric stability regimes," Wind Energy 23, 501–527 (2020).

¹⁶R. Barthelmie and L. Jensen, "Evaluation of wind farm efficiency and wind turbine wakes at the Nysted offshore wind farm," Wind Energy 13, 573–586 (2010).

¹⁷K. Hansen, R. Barthelmie, L. Jensen, and A. Sommer, "The impact of turbulence intensity and atmospheric stability on power deficits due to wind turbine wakes at Horns Rev wind farm," Wind Energy 15, 183–196 (2012).

¹⁸ A. R. Meyer Forsting, N. Troldborg, and M. Gaunaa, "The flow upstream of a row of aligned wind turbine rotors and its effect on power production," Wind Energy 20, 63–77 (2017).

- ¹⁹K. L. Wu and F. Porté-Agel, "Flow adjustment inside and around large finite-size wind farms," Energies 10, 2164 (2017).
- ²⁰R. Ebenhoch, B. Muro, J. Å. Dahlberg, P. Berkesten Hägglund, and A. Segalini, "A linearized numerical model of wind-farm flows," Wind Energy 20, 859–875 (2017).
- ²¹J. Bleeg, M. Purcell, R. Ruisi, and E. Traiger, "Wind farm blockage and the consequences of neglecting its impact on energy production," Energies 11, 1609 (2018).
- ²²E. Branlard, E. Quon, A. R. Meyer Forsting, J. King, and P. Moriarty, "Wind farm blockage effects: Comparison of different engineering models," J. Phys.: Conf. Ser. 1618, 062036 (2020).
- ²³J. Schneemann, F. Theuer, A. Rott, M. Dörenkämper, and M. Kühn, "Offshore wind farm global blockage measured with scanning lidar," Wind Energy Sci. 6, 521–538 (2021).
- 24T. Nishino and R. H. J. Willden, "The efficiency of an array of tidal turbines partially blocking a wide channel," J. Fluid Mech. 708, 596–606 (2012).
- 25 S. McTavish, S. Rodrigue, and D. Feszty, "An investigation of in-field blockage effects in closely spaced lateral wind farm configurations," Wind Energy 18, 1989–2011 (2014).
- ²⁶N. O. Jensen, "A note on wind generator interaction," Technical Report No. 2411 (Risø, Roskilde, Denmark, 1983).
- ²⁷S. Frandsen, R. Barthelmie, S. Pryor, O. Rathmann, S. Larsen, J. Højstrup, and M. Thøgersen, "Analytical modelling of wind speed deficit in large offshore wind farms," Wind Energy 9, 39–53 (2006).
- 28H. Schlichting, Boundary Layer Theory, 9th ed. (McGraw-Hill, 1979), p. 799.
- ²⁹G. N. Abramovich, *The Theory of Turbulent Jets* (MIT Press, 1963), p. 677.

 ³⁰P. Lissaman, "Energy effectiveness of arbitrary arrays of wind turbines
- ³⁰P. Lissaman, "Energy effectiveness of arbitrary arrays of wind turbines," J. Energy 3, 323–328 (1979).
- 31S. Voutsinas, "On the analysis of wake effects in wind parks," Wind Eng. 14, 204–219 (1990).
- ³²G. Larsen, "A simple wake calculation procedure," Technical Report No. 2760 (Technical University of Denmark, Roskilde, Denmark, 1988).
- 33M. Bastankhah and F. Porté-Agel, "A new analytical model for wind-turbine wakes," Renewable Energy 70, 116–123 (2014).
- 34T. Ishihara and G. W. Qian, "A new Gaussian-based analytical wake model for wind turbines considering ambient turbulence intensities and thrust coefficient effects," J. Wind Eng. Ind. Aerodyn. 177, 275–292 (2018).
- 35S. Xie and C. Archer, "Self-similarity and turbulence characteristics of wind turbine wakes via large-eddy simulation," Wind Energy 18, 1815–1838 (2015).
- 36W. C. Cheng and F. Porté-Agel, "A simple physically-based model for wind-turbine wake growth in a turbulent boundary layer," Boundary-Layer Meteorol. 169, 1-10 (2018).
- ³⁷J. Schreiber, A. Balbaa, and C. L. Bottasso, "Brief communication: A double-Gaussian wake model," Wind Energy Sci. 5, 237–244 (2020).
- ³⁸C. R. Shapiro, G. M. Starke, C. Meneveau, and D. F. Gayme, "A wake modeling paradigm for wind farm design and control," Energies **12**, 2956 (2019).
- ³⁹F. Blondel and M. Cathelain, "An alternative form of the super-Gaussian wind turbine wake model," Wind Energy Sci. 5, 1225–1236 (2020).
- 40 S. B. Pope, *Turbulent Flows* (Cambridge University Press, 2000), p. 773.
- ⁴¹G. Crasto, A. R. Gravdahl, F. Castellani, and E. Piccioni, "Wake modeling with the actuator disc concept," Energy Procedia 24, 385–392 (2012).
- ⁴²N. G. Mortensen, "Wind resource assessment using the WAsP software," Technical Report No. 0135 (DTU Wind Energy E-0135, 2016).
- ⁴³P. M. Gebraad, F. Teeuwisse, J. Van Wingerden, P. A. Fleming, S. Ruben, J. Marden, and L. Pao, "Wind plant power optimization through yaw control using a parametric model for wake effects-a CFD simulation study," Wind Energy 19, 95–114 (2016).
- ⁴⁴L. Zhan, S. Letizia, and G. V. Iungo, "Optimal tuning of engineering wake models through lidar measurements," Wind Energy Sci. 5, 1601–1622 (2020).
- ⁴⁵K. Gunn, C. Stock-Williams, M. Burke, R. Willden, C. Vogel, W. Hunter, T. Stallard, N. Robinson, and S. R. Schmidt, "Limitations to the validity of single wake superposition in wind farm yield assessment," J. Phys.: Conf. Ser. 749, 012003 (2016).
- ⁴⁶H. Zong and F. Porté-Agel, "A momentum-conserving wake superposition method for wind farm power prediction," J. Fluid Mech. 889, A8 (2020).

- ⁴⁷R. Barthelmie, L. Folkerts, G. C. Larsen, K. Rados, S. C. Pryor, S. Frandsen, B. Lange, and G. Schepers, "Comparison of wake model simulations with offshore wind turbine wake profiles measured by sodar," J. Atmos. Oceanic Technol. 23, 888–901 (2006).
- ⁴⁸R. J. Barthelmie, K. Hansen, S. T. Frandsen, O. Rathmann, J. G. Schepers, W. Schlez, J. Phillips, K. Rados, A. Zervos, E. S. Politis, and P. K. Chaviaropoulos, "Modelling and measuring flow and wind turbine wakes in large wind farms offshore," Wind Energy 12, 431–444 (2009).
- ⁴⁹P. Moriarty, J. S. Rodrigo, P. Gancarski, M. Chuchfield, J. W. Naughton, K. S. Hansen, E. MacHefaux, E. Maguire, F. Castellani, L. Terzi, S. P. Breton, and Y. Ueda, "IEA-task 31 WAKEBENCH: Towards a protocol for wind farm flow model evaluation. Part 2: Wind farm wake models," J. Phys.: Conf. Ser. 524, 012185 (2014).
- ⁵⁰C. L. Archer, A. Vasel-Be-Hagh, C. Yan, S. Wu, Y. Pan, J. F. Brodie, and A. E. Maguire, "Review and evaluation of wake loss models for wind energy applications," Appl. Energy 226, 1187–1207 (2018).
- ⁵¹C. Santoni, E. J. Garcia-Cartgena, U. Ciri, G. V. Iungo, and S. Leonardi, "Coupling of mesoscale weather research and forecasting model to a high fidelity large Eddy simulation," J. Phys.: Conf. Ser. 1037, 062010 (2018).
- ⁵²C. Santoni, E. J. Garcia-Cartgena, U. Ciri, L. Zhan, G. V. Iungo, and S. Leonardi, "One-way mesoscale-microscale coupling for simulating a wind farm in North Texas: Assessment against SCADA and LiDAR data," Wind Energy 23, 691–710 (2020).
- ⁵³D. Mehta, A. H. V. Zuijlen, B. Koren, J. G. Holierhoek, and H. Bijl, "Large Eddy Simulation of wind farm aerodynamics: A review," J. Wind Eng. Ind. Aerodyn. 133, 1–17 (2014).
- 54Breton, S., Sumner, J., Sørensen, J., Hansen, K., Sarmast, S., and Ivanell, S., "A survey of modelling methods for high-fidelity wind farm simulations using large eddy simulation," Philos Trans. R. Soc. A 375, 20160097 (2017).
- 55B. Sanderse, S. Van Der Pijl, and B. Koren, "Review of computational fluid dynamics for wind turbine wake aerodynamics," Wind Energy 14, 799–819 (2011).
- 56E. Bou-Zeid, C. Meneveau, and M. Parlange, "A scale-dependent Lagrangian dynamic model for large eddy simulation of complex turbulent flows," Phys. Fluids 17, 025105 (2005).
- ⁵⁷F. Wan and F. Porté-Agel, "Large-Eddy simulation of stably-stratified flow over a steep hill," Boundary-Layer Meteorol. 138, 367–384 (2011).
- 58 M. P. Van Der Laan, N. N. Sørensen, P.-E. Réthoré, J. Mann, M. C. Kelly, N. Troldborg, J. G. Schepers, and E. Machefaux, "An improved $\kappa \varepsilon$ model applied to a wind turbine wake in atmospheric turbulence," Wind Energy 18, 889–907 (2015).
- ⁵⁹P. A. Taylor, "On wake decay and row spacing for WECS farms," in 3rd International Symposium on Wind Energy Systems (BHRA, 1980), pp. 451-468.
- ⁶⁰P. M. Sforza, P. Sheerin, and M. Smorto, "Three-dimensional wakes of simulated wind turbines," AIAA J. 19, 1101–1107 (1981).
- ⁶¹ A. Crespo, F. Manuel, D. Moreno, E. Fraga, and J. Hernandez, "Numerical analysis of wind turbine wakes," in *Proceedings of an International Workshop Held at the European Culture Center of Delphi, Greece* (1985), pp. 15–25.
- ⁶²S. Ott, J. Berg, and M. Nielsen, "Linearised CFD models for wakes," Technical Report No. 1772 (Risø, Roskilde, Denmark, 2011).
- ⁶³L. A. Martínez-Tossas, J. Annoni, P. A. Fleming, and M. J. Churchfield, "The aerodynamics of the curled wake: A simplified model in view of flow control," Wind Energy Sci. 4, 127–138 (2019).
- ⁶⁴M. K. Liu, M. A. Yocke, and T. C. Myers, "Mathematical model for the analysis of wind-turbine wakes," J. Energy 7, 73–78 (1983).
- 65J. Ainslie, "Calculating the flow field in the wake of wind turbines," J. Wind Eng. Ind. Aerodyn. 27, 213–224 (1988).
- ⁶⁶G. V. Iungo, F. Viola, U. Ciri, M. A. Rotea, and S. Leonardi, "Data-driven RANS for simulations of large wind farms," J. Phys.: Conf. Ser. **625**, 012025 (2015).
- ⁶⁷G. V. Iungo, V. Santhanagopalan, U. Ciri, F. Viola, L. Zhan, M. A. Rotea, and S. Leonardi, "Parabolic RANS solver for low-computational-cost simulations of wind turbine wakes," Wind Energy 21, 184–197 (2017).
- ⁶⁸V. Santhanagopalan, M. A. Rotea, and G. V. Iungo, "Performance optimization of a wind turbine column for different incoming wind turbulence," Renewable Energy 116, 232–243 (2018).

- ⁶⁹P. Bradstock and W. Schlez, "Theory and verification of a new 3D RANS wake model," Wind Energy Sci. 5, 1425–1434 (2020).
- 70 L. Martínez-Tossas, J. King, E. Quon, C. Bay, R. Mudafort, N. Hamilton, and P. Fleming, "The curled wake model: A three-dimensional and extremely fast steady-state wake solver for wind plant flows," Wind Energy Sci. 6, 555–570 (2021)
- ⁷¹A. Crespo and J. Hendández, "Parabolic and elliptic models of wind turbine wakes. application to the interaction between different wakes and turbines," J. Comput. Fluid Dyn. 4, 104–127 (1991).
- ⁷²C. Masson, I. Ammara, and I. Paraschivoiu, "An aerodynamic method for the analysis of isolated horizontal-axis wind turbines," Int. J. Rotating Mach. 3, 21–32 (1997).
- ⁷³C. Leclerc, C. Masson, and I. Ammara, "Turbulence modeling of the flow around horizontal axis wind turbines," Wind Eng. 23, 279–294 (1999).
- 74I. Ammara, C. Leclerc, and C. Masson, "A viscous three-dimensional differential/actuator-disk method for the aerodynamic analysis of wind farms," J. Sol. Energy Eng. 124, 345 (2002).
- 75M. Soleimanzadeh, R. Wisniewski, and A. Brand, "State-space representation of the wind flow model in wind farms," Wind Energy 17, 627–639 (2014).
- ⁷⁶J. Annoni and P. Seiler, "A low-order model for wind farm control," Proceedings of the American Control Conference (IEEE, 2015), pp. 1721–1727.
- ⁷⁷R. King, P. Hamlington, K. Dykes, and P. Graf, "Adjoint optimization of wind farm layouts for systems engineering analysis," in 34th Wind Energy Symposium (AIAA, 2016), p. 2199.
- ⁷⁸C. Adcock and R. King, "Data-driven wind farm optimization incorporating effects of turbulence intensity," in *Annual American Control Conference* (IEEE, Wisconsin Center, Milwaukee, WI, 2018), pp. 1–6.
- ⁷⁹R. King, K. Dykes, P. Graf, and P. Hamlington, "Optimization of wind plant layouts using an adjoint approach," Wind Energy Sci. 2, 115–131 (2017).
- ⁸⁰G. Larsen, "Wake meandering: A pragmatic approach," Wind Energy 11, 377–395 (2008).
- ⁸¹R. E. Keck, D. Veldkamp, H. A. Madsen, and G. Larsen, "Implementation of a mixing length turbulence formulation into the dynamic wake meandering model," J. Sol. Energy Eng. 134, 021012 (2012).
- 82J. Boussinesq, Théorie de L'écoulement Tourbillonnant et Tumultueux Des Liquides Dans Les Lits Rectilignes a Grande Section (Gauthier-Villars, 1897), Vol. 1.
- 83R. Gómez-Elvira, A. Crespo, E. Migoya, F. Manuel, and J. Hernández, "Anisotropy of turbulence in wind turbine wakes," J. Wind Eng. Ind. Aerodyn. 93, 797–814 (2005).
- 84D. Cabezón, E. Migoya, and A. Crespo, "Comparison of turbulence models for the computational fluid dynamics simulation of wind turbine wakes in the atmospheric boundary layer," Wind Energy 14, 909–921 (2011).
- ⁸⁵M. P. van der Laan, N. N. Sorensen, P.-E. Réthoré, J. Mann, M. C. Kelly, and J. G. Schepers, "Nonlinear eddy viscosity models applied to wind turbine wakes," in ICOWES2013 Conference, Copenhagen, Denmark, 17–19 June 2013, pp. 514–525.
- 86P.-E. Réthoré, "Wind turbine wake in atmospheric turbulence," Ph.D. thesis (Technical University of Denmark, 2009).
- ⁸⁷B. Lange, H. P. Waldl, A. G. Guerrero, D. Heinemann, and R. J. Barthelmie, "Modelling of offshore wind turbine wakes with the wind farm program FLaP," Wind Energy 6, 87–104 (2003).
- ⁸⁸R. Keck, R. Mikkelsen, N. Troldborg, M. de Maré, and K. S. Hansen, "Synthetic atmospheric turbulence and wind shear in large eddy simulations of wind turbine wakes," Wind Energy 17, 1247–1267 (2014).
- 89 R. Keck, M. de Maré, M. Churchfield, S. Lee, G. Larsen, and H. Madsen, "Two improvements to the dynamic wake meandering model: Including the effects of atmospheric shear on wake turbulence and incorporating turbulence build-up in a row of wind turbines," Wind Energy 18, 111–132 (2015).
- ⁹⁰G. V. Iungo, S. Letizia, and L. Zhan, "Quantification of the axial induction exerted by utility-scale wind turbines by coupling LiDAR measurements and RANS simulations," J. Phys.: Conf. Series 1037, 072023 (2018).
- ⁹¹J. M. Prospathopoulos, E. S. Politis, K. G. Rados, and P. K. Chaviaropoulos, "Evaluation of the effects of turbulence model enhancements on wind turbine wake predictions," Wind Energy 14, 285–300 (2011).
- 92 A. E. Kasmi and C. Masson, "An extended k-ε model for turbulent flow through horizontal-axis wind turbines," J. Wind Eng. Ind. Aerodyn. 96, 103–122 (2008).

- ⁹³M. P. Van Der Laan, K. S. Hansen, N. N. Sørensen, and P. E. Réthoré, "Predicting wind farm wake interaction with RANS: An investigation of the Coriolis force," J. Phys.: Conf. Ser. 625, 012026 (2015).
- ⁹⁴J. Hennen and S. Kenjereš, "Contribution to improved eddy-viscosity modeling of the wind turbine-to-wake interactions," Int. J. Heat Fluid Flow 68, 319–336 (2017).
- 95 M. P. Van Der Laan, S. J. Andersen, M. Kelly, and M. C. Baungaard, "Fluid scaling laws of idealized wind farm simulations," J. Phys.: Conf. Ser. 1618, 062018 (2020)
- ⁹⁶L. Cea, J. Puertas, and V.-C. M. E, "Depth averaged modelling of turbulent shallow water flow with wet-dry fronts," Arch. Comput. Methods Eng. 14, 303–341 (2007).
- ⁹⁷G. V. Iungo, F. Viola, S. Camarri, F. Porté-Agel, and F. Gallaire, "Linear stability analysis of wind turbine wakes performed on wind tunnel measurements," J. Fluid Mech. 737, 499–526 (2013).
- 98J. Meyers and C. Meneveau, "Large eddy simulations of large wind-turbine arrays in the atmospheric boundary layer," in AIAA Paper No. AIAA 2010-827, 2010.
- ⁹⁹D. Medici and P. H. Alfredsson, "Measurements on a wind turbine wake: 3D effects and bluff body vortex shedding," Wind Energy 9, 219–236 (2006).
- effects and bluff body vortex shedding," Wind Energy **9**, 219–236 (2006). ¹⁰⁰L. P. Chamorro and F. Porté-Agel, "A wind-tunnel investigation of wind-turbine wakes: Boundary-layer turbulence effects," Boundary-Layer Meteorol. **132**, 129–149 (2009).
- 101S. Boersma, B. Doekemeijer, M. Vali, J. Meyers, and J-Wv. Wingerden, "A control-oriented dynamic wind farm model: WFSim," Wind Energy Sci. 3, 75–95 (2018).
- 102R. H. Pletcher, J. C. Tannehill, and D. Anderson, Computational Fluid Mechanics and Heat Transfer (CRC Press, 2012).
- 103V. S. Pratap and D. B. Spalding, "Numerical computations of the flow in curved ducts," Aeronaut. Quart. 3, 219–228 (1975).
- 104W. R. Briley, "Numerical method for predicting three-dimensional steady viscous flow in ducts," J. Comput. Phys. 28, 8–28 (1974).
- 105 J. Moore and J. G. Moore, "Calculation procedure for three-dimensional, viscous, compressible duct flow—1. Inviscid flow considerations," ASTM Spec. Tech. Publ. 101, 75–82 (1979).
- 106P. R. Dodge, "Numerical method for 2D and 3D viscous flows," AIAA J. 15, 961–965 (1977).
- 107R. Chilukuri and R. H. Pletcher, "Numerical solutions to the partially parabolized Navier-Stokes equations for developing flow in a channel," Numer. Heat Transfer 3, 169–188 (1980).
- 108S. Haglund El Gaidi, "Partially parabolic wind turbine flow modelling," M.S. thesis (Royal Institute of Technology, 2018).
- 109 J. Y. Murthy and S. V. Patankar, "A partially parabolic calculation procedure for duct flows in irregular geometries: Part L: Formulation," Numer. Heat Transfer, Part B 16, 1-15 (1990).
- ¹¹⁰R. Maulik, V. Rao, A. Renganathan, S. Letizia, and G. V. Iungo, "Cluster analysis of wind turbine wakes measured through a scanning Doppler wind LiDAR," in AIAA Paper No. AIAA 2021-1181, 2021.
- ^{III}H. Beck and M. Kühn, "Dynamic data filtering of long-range Doppler LiDAR wind speed measurements," Remote Sens. 9, 561 (2017).
- ¹¹²International Electrotechnical Commission, "Wind energy generation systems—Part 12-1: Power performance measurements of electricity producing wind turbines," Standard No. 61400-12-2 (International Electrotechnical Commission, Geneva, Switzerland, 2017).
- ¹¹³International Electrotechnical Commission, "Wind turbine generator systems—Part 12-2: Power performance of electricity-producing wind turbines based on nacelle anemometry," Standard No. 61400-12-2 (International Electrotechnical Commission, Geneva, Switzerland, 2013).
- ¹¹⁴N. Hamilton, C. J. Bay, P. Fleming, J. King, and L. A. Martínez-Tossas, "Comparison of modular analytical wake models to the Lillgrund wind plant," J. Renewable Sustainable Energy 12, 053311 (2020).
- ¹¹⁵J. Teng and C. D. Markfort, "A calibration procedure for an analytical wake model using wind farm operational data," Energies 13, 3537 (2020).
- ¹¹⁶S. Letizia, L. Zhan, and G. Valerio Iungo, "LiSBOA: LiDAR Statistical Barnes Objective Analysis for optimal design of LiDAR scans and retrieval of wind statistics. Part I: Theoretical framework," Atmos. Meas. Tech. 14, 2065–2093 (2021).
- 117S. Letizia, L. Zhan, and G. Valerio Iungo, "LiSBOA: LiDAR Statistical Barnes Objective Analysis for optimal design of LiDAR scans and retrieval of wind

- statistics. Part II: Applications lidar measurements of wind turbine wakes," Atmos. Meas. Tech. 14, 2095-2113 (2021).
- 118 See https://www.mathworks.com/matlabcentral/fileexchange/4551-inpaint_nans for "inpaint_nans.m, Matlab File Exchange Community Website" (2021) (last accesed July 30, 2021).
- ¹¹⁹P. E. J. Vermeulen, "An experimental analysis of wind turbine wake," in Third International Symposium on Wind Energy Systems, Copenhagen, 1980.
- 120 L. P. Chamorro, M. Guala, R. E. Arndt, and F. Sotiropoulos, "On the evolution of turbulent scales in the wake of a wind turbine model," J. Turbul. 13, N27 (2012).
- ¹²¹AIAA, "Guide for the verification and validation of computational," Technical Report No. G-077 (American Institute of Aeronautics and Astronautics, 2002).
- 122 F. Viola, G. V. Iungo, S. Camarri, F. Porté-Agel, and F. Gallaire, "Prediction of the hub vortex instability in a wind turbine wake: Stability analysis with eddyviscosity models calibrated on wind tunnel data," J. Fluid Mech. 750, R1
- 123 See https://github.com/UTD-WindFluX/G-RANS for "UTD WindFluX Global RANS Solver for Simulations of Axisymmetric Wind Turbine Wakes" (last accessed October 27, 2021).
- 124 E. Machefaux, G. C. Larsen, and J. P. Leon, "Engineering models for merging wakes in wind farm optimization applications," J. Phys.: Conf. Ser. 625, 012037 (2015).

- 125 K. Walker, N. Adams, B. Gribben, B. Gellatly, N. G. Nygaard, A. Henderson, M. Marchante Jimémez, S. R. Schmidt, J. Rodriguez Ruiz, D. Paredes, G. Harrington, N. Connell, O. Peronne, M. Cordoba, P. Housley, R. Cussons, M. Håkansson, A. Knauer, and E. Maguire, "An evaluation of the predictive accuracy of wake effects models for offshore wind farms," Wind Energy 19, 979-996 (2016).
- A. Farrell, J. King, C. Draxl, R. Mudafort, N. Hamilton, C. J. Bay, P. Fleming, and E. Simley, "Design and analysis of a wake model for spatially heterogeneous flow," Wind Energy Sci. 6, 737-758 (2021).
- ¹²⁷ A. J. Wheeler and R. J. Ahmad, Introduction to Engineering Experimentation (Pearson Higher Education, New Jersey, 2004).
- ¹²⁸N. G. Nygaard, "Systematic quantification of wake model uncertainty," in EWEA Offshore, 2015.
- 129A. Niayifar and F. Porté-Agel, "Analytical modeling of wind farms: A new approach for power prediction," Energies 9, 741 (2016).

 130 NREL, see https://population.un.org/wpp/Graphs/DemographicProfiles/Line/
- 900 for "Floris. Version 2.4" (2021) (last accessed September 1, 2021).
- 131 A. Niayifar and F. Porté-Agel, "A new analytical model for wind farm power
- prediction," J. Phys.: Conf. Ser. **625**, 012039 (2015).

 1328. V. Patankar and D. B. Spalding, "A calculation procedure for heat, mass and momentum transfer in three-dimensional parabolic flows," Int. J. Heat Mass Transfer 15, 1787-1806 (1972).